國立交通大學

環境工程研究所

碩士論文

多孔性硫酸化二氧化鋯結構與表面酸性對質子導度影響之研究

Texture and Surface Acidity Dependent Proton Conductivities of Porous Sulfated Zirconia

研究生：古芝萍

指導教授：張淑閔　副教授

中華民國一百零一年一月

多孔性硫酸化二氧化鋯結構與表面酸性對質子導度影響之研究

Texture and Surface Acidity Dependent Proton Conductivities of Porous Sulfated Zirconia

研究生：古芝萍　　Student：Jhih-Ping Gu

指導教授：張淑閔　　Advisor：Sue-Min Chang

國立交通大學
環境工程研究所
碩士論文

A Thesis
Submitted to Institute of Environmental Engineering
College of Engineering
National Chiao Tung University
In partial Fulfillment of the Requirements
for the Degree of
Master
In

Environmental Engineering

January 2012

Hsinchu, Taiwan, Republic of China

中華民國一百零一年一月

中文摘要

在本文研究，我們製備了多孔性的硫酸化二氧化鋯並且應用其特性在質子交換膜燃料電池中質子傳導膜的基材。除了檢測其材料的多孔結構性質及表面酸度外，並加以討論此兩者的相互關係及兩者對質子導度的單方及相互的影響。製備多孔結構的硫酸化二氧化鋯，是利用不同長碳鏈的介面活性劑當作模板以共沉澱法或水熱法合成。中孔洞硫酸化二氧化鋯隨著界面活性劑的增加，其比表面積從 78 增加至 128 m^2/g，相對的質子導度也從 1.2×10^{-2} 提升至 2.0×10^{-2} S/cm。微孔洞硫酸化二氧化鋯有較高的質子導度約 2.6×10^{-2} S/cm。推測其微孔的小孔徑及其高的表面酸度使得質子易在表面傳遞。而利用中孔洞硫酸化二氧化鋯(C_{16}TAB/Zr= 0.5, average pore size= 2.8, surface area= 128 m^2/g)的樣品用 0.9M 的硫酸溶液做再披覆後發現，質子導度提升為原本 2.0×10^{-2} S/cm 至 9.5×10^{-2} S/cm，且此數值比現今商業質子交換膜(Nafion, 5.2×10^{-2} S/cm)之效益高約兩倍。孔徑大小與表面酸性皆影響著水含量並且控制著質子傳導的能力。即便微孔洞的硫酸化二氧化鋯有著最高的水分吸附能力，但其質子導度卻並沒有如經過再披覆硫酸的樣品來的高，推測小於 0.6 nm 的微孔洞材料，水分會因為太緊密的吸附在表面而導致質子不易傳導，因此適當的孔徑大小和表面酸性結合可使材料具有高的質子導度特性。

Abstract

In this study, porous sulfated ZrO_2 (S-ZrO_2) powders were prepared as a promising alternative proton-conducting material for fuel cells. The porous structure, surface acidity and proton conductivity were examined and their relationships were investigated. The S-ZO_2 samples were prepared through templating precipitation and hydrothermal method. The mesoporous S-ZrO_2 samples exhibited the proton conductivities of 1.2-2.0×10^{-2} S/cm, and the conductivities were highly dependent on their specific surface areas (78-128 m^2/g). The microporous S-ZrO_2 sample templated with octyltrimethylammonium bromide (C_8TAB) had a higher proton conductivity of 2.6 ×10^{-2} S/cm. Small pore sizes assist protons hopping between bulk water and surface acidic sites to promote conductive efficiency. Post impregnation of the mesoporous S-ZrO_2 sample ($C_{16}TAB/Zr$= 0.5, average pore size= 2.8, surface area= 128 m^2/g) with a 0.9 M H_2SO_4 solution remarkably improved its proton conductivity from 2.0 ×10^{-2} to 9.5 ×10^{-2} S/cm. This value is twice higher than that of the commercial Nafion (5.2×10^{-2} S/cm). Both the pore size and surface acidity determine the water content and control the proton conductivity. Even though the microporous S-ZrO_2 samples showed the highest capability for keeping water molecules, their proton conductivity were not higher than the post sulfation powders. Microporous channels with the pore size smaller than 0.6 nm block water tightly and retard proton diffusion. Therefore, the optimal pore size (0.6-2.8nm) and surface acidity can contribute to high proton conductivity.

謝誌

當碩士論文列印成完整的一本時，凝視著它，頓時回想起裡面的內容種種，不知包含了多少人的協助與關愛，油然而生的是無法言喻的感謝，沒有你們沒有這一本論文，這才知道每一本論文裡除了本身的學術價值外，最最珍貴的莫過於無價的人情。承蒙指導教授　張淑閔老師敦敦教誨，無論是學習研究，人情世故皆受益良多，老師的一句話永遠銘記在心，「這是人生的課題，勇於面對，不輕易放棄！」，研究歷程，所受心志與知識能力的磨練皆仰賴這句話而支持到最後。感謝交大材料系　吳樸偉教授的指導，深入淺出的教學，開啟了我在電化學的興趣與視野，也謝謝教授在專業領域上給予幫助，當遇到瓶頸時也在旁提供建議。謝謝　楊昌中博士，在研討會上為我開啟了不同研究領域上的門，拓展了我更多對於研究上的認識，以及對論文的悉心指正。政男舅舅在大學即將結束時，給了我一個研究所的夢及目標，在研究所過程中，也扮演著時時提點的教師，陪伴著我成長直到最後。隔行如隔山，在剛進入實驗室時，深深體悟這句話，還記得一開始對研究如此懵懂無知，因生疏而害怕時，品欣學姊如天使般的教導與關愛，帶我度過了最初最艱難的時刻，不僅僅訓練我能獨當一面，還提醒了我社會的黑暗面。實驗室裡的大哥哥，胥哥，樹立了一個好榜樣讓我學習著，對於研究應有什麼樣的學習程度，對於生活應有什麼樣的看待方式。兩位同儕，Ian 跟 Ashley 也扮演著學習上的玩伴，對於我有許多的關愛與包容。兩位學弟，Jeremy 和 Jason 在我忙碌無力時也不時地給予幫忙，很感謝實驗室的各位一路的陪伴。學術研究上，許多學長就像是走在前面的大人，提領著我，帶著我學習，幫助我研究，非常謝謝錦貞、聖鑫、世民、亮毅、晨宏眾學長們。明青、宇君、建龍及損友們，常常是我吐苦水的對象，沒有你們我應該就像是即將爆裂的氣球一樣危險，謝謝你們不時地替我放放氣。嫒心也常常如神來一筆的，在我急需幫助時，突然的出現伸出援手。最後我最親愛的家人，尤其是媽媽、阿婆、小君姐、哥哥，雖然你們如霧裡看花的看著我學習，但在給我的溫飽的愛心便當裡，我看見你們用你們的方式關心，每吃一口都讓我更有力氣向前！此外要感謝的人太多了，不如就謝天吧！

芝萍　謹誌　中華民國一百零一年一月

Content Index

Figure Index

Table Index

Chapter 1. Introduction

1-1. Motivation

Environment issue is vital to global prosperity. Driving the global ecological system into a sustainable path is progressively becoming a major concern and policy objective. Fuel cell is an electrochemical device that generates power with zero emission, quiet and highly efficient more than fuel burning. Nowadays, it was considered to be one of the clean power source devices. The classification determines the kind of electrolyte substance take place in the fuel cell, and other factors. There are several types of fuel cells such as Proton exchange membrane (PEM), Direct methanol, Alkaline, Phosphoric acid, Molten carbonate, Solid oxide, Regenerative fuel cells. Especially the proton exchange membrane fuel cell (PEMFC) has large potential for light duty vehicles and portable applications.

The properties of the PEM[1, 2] such as proton conductivity strongly effect performance of PEMFC. The function of the PEM in a fuel cell is to effectively separate the anode and cathode electrodes as well as facilitate the conduction of protons. The first requirement implies that the membrane must possess chemical, thermal, and morphological stability and little or no gas permeability over a variety of operating conditions. Nafion[3-5] is a commercial polymer membrane mostly used as the solid electrolyte for PEMFC. For the requirement of efficiency working environment, the relative high temperature is needed. However, Nafion have been shown that the proton conductivity decreases at elevated temperatures[6, 7]. Numerous efforts have been devoted to synthesize polymers including the Nafion-based composites[8, 9] and per-fluorinated polymers[10] to improve the disadvantage of Nafion. Other attentions of research have been focused on the inorganic materials, which have several properties that may be beneficial for their use as possible solid-state electrolyte alternatives. The electrochemical performance films of metal oxides have been the subject, due to the acidity on the surface, such as SiO_2[11], TiO_2[12], ZrO_2[13], binary and ternary mixtures of TiO_2 with other oxides[14]. Numerous studies have shown that the surface acidity of metal oxides has good performance to transport proton. Especially, Sulfated ZrO_2[15], a super solid acid, exhibits H_0 (Hammett acid strength) of -16.03 represent that protons were very easily released from the surface. It shows the lowest value of H_0 than the other metal oxides and also Nafion ($H_0 = -12$). Therefore, it has been demonstrated to exhibit high proton conductivity. Numerous studies have been shown the structure of sulfated ZrO_2 and found out the good ability of transport proton was because of its Brønsted and Lewis acid sites[16].

Most inorganic materials would be formed like porous structure with large internal surface area and pore channel[17]. It was consider that the more acid site and the texture help the proton transportation and water content. Nogami et al.[11] found out positive linearly relation between the surface area and the reciprocal number of the pore radius with conductivity, however, the definite range of the pore radius was not to be indicated directly. In Yamada et al.[18] and Marschall et al.[6] studies, they had mentioned about the narrowed pore channels (2nm ~ 5nm) may be helpful for protons transport. Hara et al.[19] reported that hydrated tin dioxide and hydrated zirconia had many micropores with a pore radius below 1 nm. Both of them had high proton conductivity approximately 10^{-2} Scm^{-1} at 150°C under 95% relative humidity.

Upon previous studies, mesoporous or microporous sulfated ZrO_2 is a material which combines both benefit of surface acidity and morphology. Although there were many efforts work had been studies about porous sulfated ZrO_2 with high proton conductivity[19]. However, there still have a functional relation between surface acidity and morphology, both of them have relative contribution to proton conductivity. The affection of proton conductivity should be discussed by these two factors separately.

1-2. Objectives

In this study, we prepared different porous sulfated zirconia, which has a high proton conductivity using templating precipitation and hydrothermal method. The proton conductivity further insight into pore structure by exploring the changes in conductivity with various pore sizes of different preparations, the observed trends have been found to give insight into the conductivity with respect to various types of porous structure. The form in which sulfate groups are present at the surface of porous sulfated zirconia in various proton transfer ability. Various spectroscopic will be used to indicate the possible formation to find out the relation between the chemical structures on the surface and the proton conductivity. We will discuss the functional relation between surface acidity and morphology, moreover the both affection to proton conductivity.

Chapter 2. Literature Review

2-1. Proton exchange membranes (PEMs)

2-1-1. Proton exchange membrane fuel cell (PEMFCs)

Fuel cell is a kind of electrochemical cell (Figure 2-1), which consists of three segments: the anode, the electrolyte, and the cathode. At the anode, a catalyst oxidizes the fuel, usually hydrogen, turning the fuel into a positively charged ion and a negatively charged electron. The electrolyte is specifically designed to transport the H^+ ions from the anode to the cathode. This concept of fuel cell was discovered by German scientist whose name is Christian Friedrich Schönbein in 1838. However, the first fuel cell was demonstrated by William Robert Grove just one month later, in February of 1839. The fuel cell that he made was just similar as nowadays phosphoric-acid fuel cell. Today's fuel cells are classified by different kinds of electrolyte they employ. The classification is determined by the kind of chemical reactions that take place in the cell, the kind of catalysts required, the temperature range in which the cell operates, the fuel required…etc. All of these characteristics affect the applications of cells strongly. Several types of fuel cells are shown in Table 2-1. Especially PEMFCs, which operate at very low temperatures of about 80°C. The efficiency of a PEM unit usually reaches between 40 to 60 per cent and electric power is up to 250 kW. Due to these characteristics, PEM units tend to be the best candidates for vehicles, buildings and smaller stationary applications.

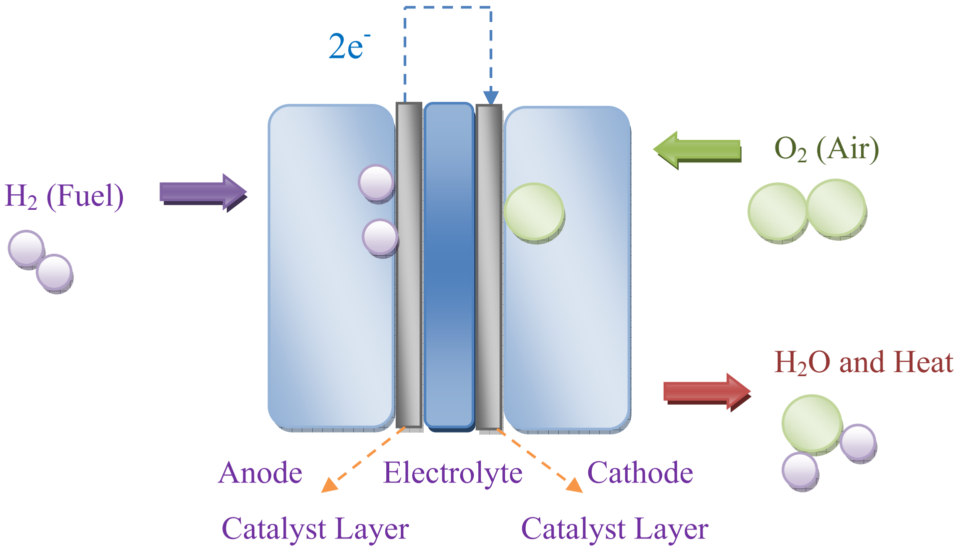

Figure 2-1 A diagram of a fuel cell

PEMFC technology was developed in the early 1960s; the first major breakthrough for PEM systems came as part of NASA’s space programme. The main objective of this project was to test the operational durability of fuel cell systems with a view to replacing batteries with fuel cells to provide electric power and drinking water to the shuttle. After decades researching, the stack was finally able to meet the performance targets for transportation application and to this day PEM technology remains the choice of the automotive industry. PEMFCs are currently used in many kinds of applications. Figure 2-2 shows the total number of PEM units installed. These data come from the web site of “fuelcelltoday.com”.

Table 2-1 Different kind of FCs [20]

Type of fuel cell	PEMFC	DMFC	SOFC	MCFC	PAFC	AFC
Electrolyte	Polymer membrane	Polymer membrane	ZrO_2	$(Li, K)_2CO_3$	H_3PO_4	KOH
Charge carrier	H^+	H^+	O^{2-}	CO_3^{2-}	H^+	OH^-
Anode	Pt/C	Pt-Ru/C	$Ni+(Zr, Y)O_2$	Ni+10wt%Cr	Pt/C	Pt/C
Cathode	Pt/C	Pt/C	$(La,Sr)MnO_3$, $LaCoO_3$	NiO	C	C
Operation temperature	30~100°C	20~80°C	600~1000°C	600~700°C	150~200°C	50~200°C
System output	1W~200kW	~0.1W~10W	~100kW	~500kW	~200kW	10kW~100kW
Usable fuels	H2、Natural Gas、Methanol	Methanol	Natural Gas、 Coal、Methanol、Petroleum	Natural Gas、Hydrogen、Carbon monoxide	Natural Gas、Methanol、Naphtha	Pure hydrogen
Advantages	*long lifetime *quick start-up *high power density	*easy to rephenish *small size/weight *high power density	*high stability *can use a variety of catalysts	*high efficiency *impure hydrogen as fuel *suitable for CHP	*high efficiency *can use impure hydrogen as fuel	*quick start-up *high performance
Disadvantages	*sensitive to fuel impurities *requires expensive catalysts	*crossover *requires expensive catalysts	*high temperature enhances breakdown of cell components *slow start-up	*slow start-up *high temperature enhances breakdown of cell components	*low current and power *large size/weight	*require pure hydrogen and oxygen
Application	Transportation、small stationary and portable power	3C products and consumer electronics	Stationary 、transportation	Electric utility and large distributed generation	Transportation	Military and Space

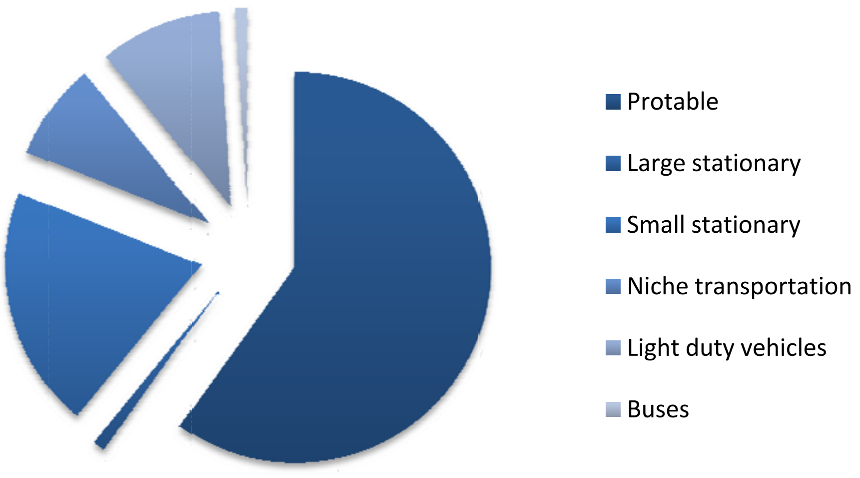

Figure 2-2 Total Number of PEM Units Installed Globally by Application [20]

2-1-2. Function of the PEM

PEM is a membrane serves as the electrolyte and completes the electrical circuit in the fuel cell. The function of the PEM in a fuel cell is to effectively separate the anode and the cathode electrodes and to facilitate the conduction of protons. The requirements for the membrane include chemical, thermal, and morphological stability and no gas permeability over a variety of operating conditions. In addition, the degree of hydration of the membrane determines the proton conductivity of PEMs. As the fuel cell is an open system with different sinks and sources for water, the chemical state and transport properties of both the water and the protonic charge carriers have to be known and to fall within defined values. These depend on the actual operating conditions such as temperature, choice of fuel, gas humidification and gas flow, the properties of the membrane/electrode interfaces, transport within the gas diffusion electrode, and electrical current drained from the fuel cell.

2-1-3. **Nafion**

Nafion[21] are copolymers of tetrafluorethylene (TFE) and perfluorinated vinyl ethers discovered in the late 1960's by Walther Grot DuPont. It is also the first synthetic polymers with ionic properties and is called an ionomer. Nafion's perfluorovinyl ether groups are terminated with sulfonate groups onto a tetrafluoroethylene backbone with ionic properties. The chemical formula is

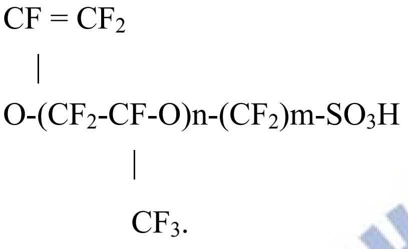

$CF = CF_2$
$|$
$O\text{-}(CF_2\text{-}CF\text{-}O)n\text{-}(CF_2)m\text{-}SO_3H$
$|$
CF_3.

Although fuel cells have been used since the 1960's as power supplies for satellites, they have received much recently attention because they provide clean energy from the reaction between H_2 and O_2. Nafion ($n = 1$, $m = 2$) was found as an effective membrane for PEMFC by permitting hydrogen ion transport while preventing electron conduction. Small angle X-ray (SAXS) and neutron scattering (SANS) data are compiled into structural models. Figure 2-3 shows two such structural models, the inverted spherical micelle model by Gierke[22] and the more disordered three-region model by Yeager et al. The top one was Gierke's suggestion of aqueous inverse spherical micelles connected by water-filled cylindrical channels. The Bottom was Yeager and Steck's three-region model of a water/ionomer mixture without regular structure. The model consists of an equal distribution of sulfonate ion clusters with a 4 nm diameter held within a continuous fluorocarbon lattice. Narrow channels about 1 nm in diameter interconnect the clusters, which explain the transport properties[3].

Water channel model[23] in Nafion is proposed based on small-angle X-ray scattering data and solid state nuclear magnetic study. In this model (Figure 2-4.), the sulfonic acid groups are self-organized into hydrophilic water channels of about 2.5 nm which is a small ion and can be easily transported. Schematic diagram of the approximately hexagonal packed several inverted-micelle cylinders. Cross-sections through the cylindrical water channels (white) and the Nafion crystallites (black) in the non-crystalline Nafion matrix (dark grey) in different kinds of PEMs

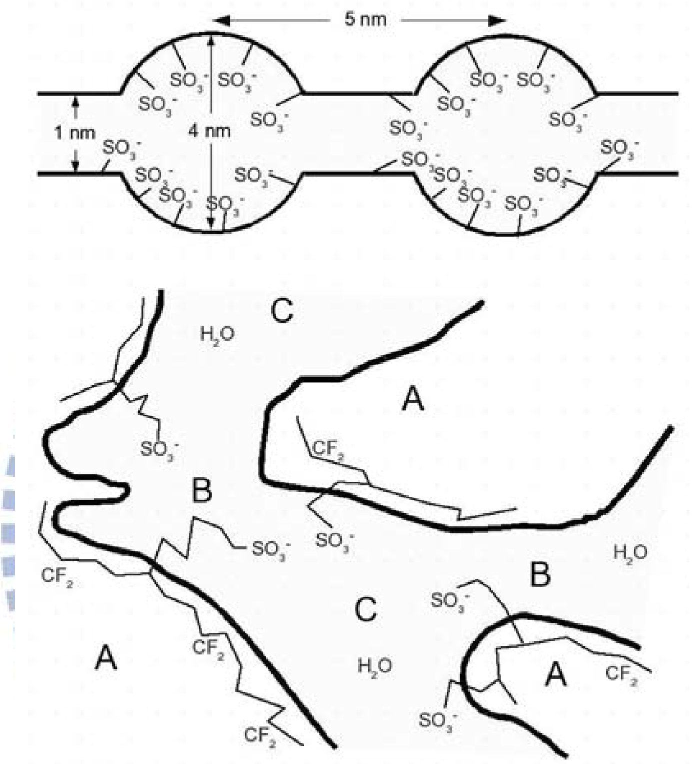

Figure 2-3 These two models were the microphases of swollen Nafion membranes. A, B and C represented the hydrophobic polymer, the solvent bridges and the hydrophilic regions, respectively.[5]

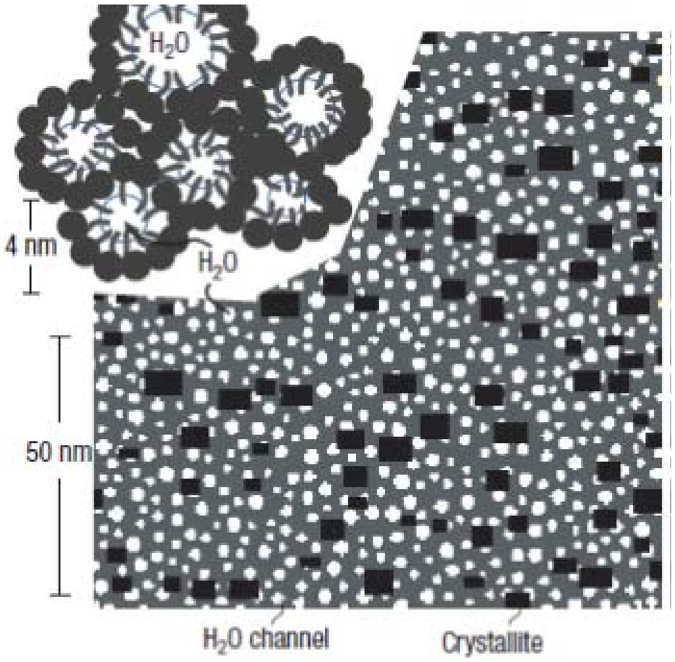

Figure 2-4 Klaus'smodel is called Parallel water-channel (inverted-micelle cylinder) of Nafion[23].

2-2. Proton Conductivity

2-2-1. Proton transfer mechanism in aqueous solution

The importance of proton transport[5] on fuel cell performances have been intensively not only for understanding the transport mechanism but also for better in designing altenative PEMs. The proton exchange membrane (PEM) plays a central role as an electrolyte for proton conduction in PEM fuel cells. Nafion is the most attractive polymeric electrolyte developed so far. It shows excellent proton conductivity. However, the high proton conductivity is only performed when the Nafion is soaked in water.

The study of proton transport[3, 24] in aqueous solution has received much attention for over a century such as in chemical, biological, and electrochemical systems. Protons in an aqueous acid exist as hydronium ions, such as $H_5O_2^+$ or $H_9O_4^+$. Eigen and De Maeyer proposed a "structure diffusion" mechanism to describe proton transport within the hydronium ions. The illustrated of the mechanism is shown in Figure 2-5. The proton which "diffuses" by hydrogen-bond breaking and forming processes. This mechanism is frequently termed "structure diffusion". The hydrogen bonds in the region of proton excess charge are contracted, and the hydrogen-bond breaking and forming processes occur in the outer portion of the complexes.

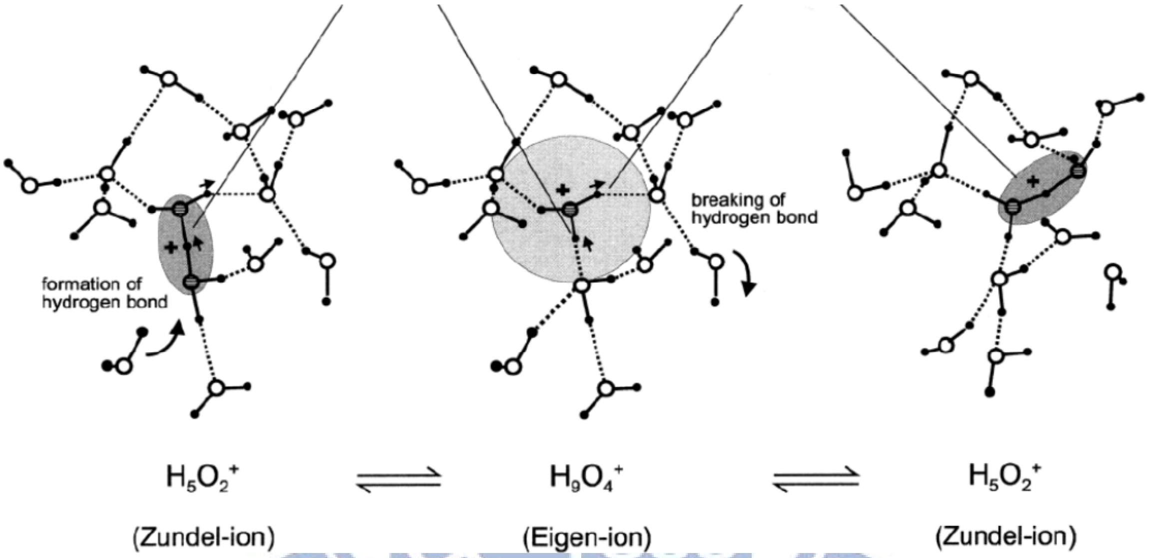

Figure 2-5 Showed Proton conduction in water.[2]

The Zundel ion acts as a proton donor through two hydrogen bonds, and each of the three outer water molecules of the Eigen ion acts as a proton donor in two hydrogen bonds and as an acceptor for the hydronium ion and an additional water molecule. These hydrogen-bond patterns through hydrogen-bond breaking and forming processes displaces in the center space and also the center of the region of excess charge. This mechanism in this type may be called "structure diffusion", because the protonic charge propagates hydrogen-bond arrangement or structure.

The mechanism of "structure diffusion" shows the cooperative phenomenon insight into the question as to what extent proton transfer in water. Another mechanism which is called “Grotthuss mechanism” (Figure 2-6) still funded diagrams showing the concerted transfer of protons within extended hydrogen-bonded water chains. The Grotthuss Mechanism is an excess proton diffuses through the hydrogen bond network of water molecules or other hydrogen-bonded liquids. The transport of protons is determined by the rate at which the hydrogen bond between a hydronium ion and a water molecule forms rather than by the slower rate at which hydronium ions may migrate, also called the vehicular mechanism.

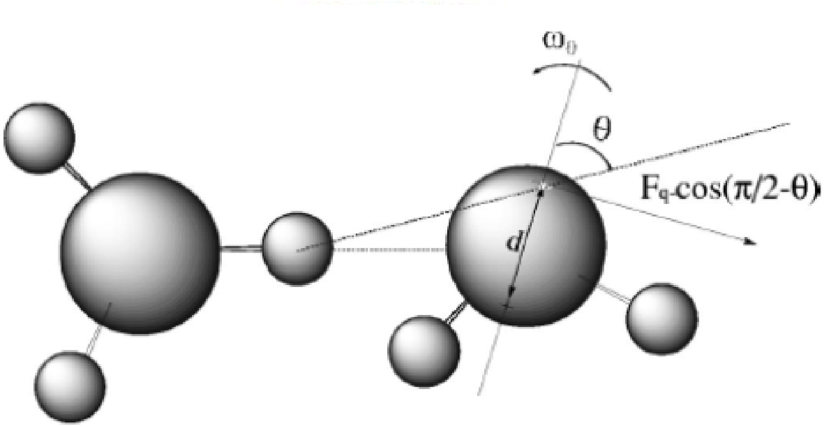

Figure 2-6 The hydrodynamic model of Grotthuss diffusion mechanism.[3]

This mechanism explains the unusual high equivalent conductivity of protons in this environment. The mobility of the proton is abnormally high as compared with other ions of a size similar to hydronium ion. However, it was pronounced that the mechanism needs to cost much energy in some references.[3] Because the creation of the corresponding dipolar moment in an unrelaxed high dielectric constant environment costs for too much energy to be consistent with a very fast process with low activation energy. The propagation mechanism of a protonic defect in a low-dimensional water structure surrounded by a low dielectric environment is obviously between “concerted” and “step-wise”; however, in bulk water, the cooperation is restricted to the dynamics of protons in neighboring hydrogen bonds.

2-2-2. Proton transfer mechanism in hydrated acidic polymer

Hydrated acidic polymers (the commercial product, Nafion) are the most commonly used separator materials for low-temperature fuel cells. Their typical nanoseparation (shown in Figure 2-7) leads to the formation of interpenetrating hydrophobic and hydrophilic domains; the hydrophobic domain gives the membrane's morphological stability, and the hydrated hydrophilic domain facilitates the conduction of protons.

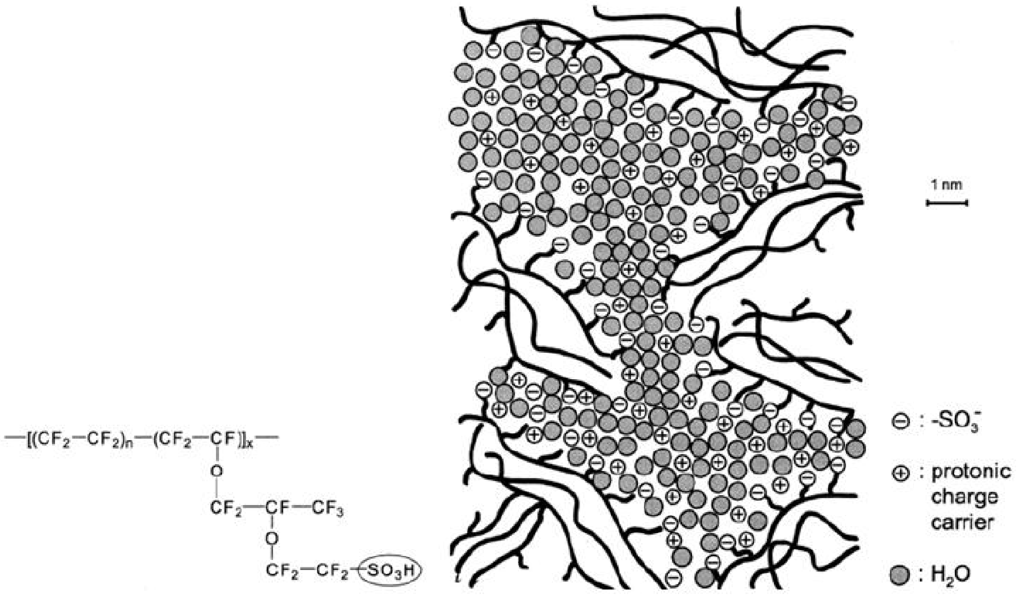

Figure 2-7 Two-dimensional illustration of some microstructural features of Nafion for an intermediate water content.[2]

There exists water content in which the middle region of the pore is referred to as "bulk water". Because the hydrophilic sulfonic acid groups are covalently bound to the hydrophobic polymer, they aggregate somewhere in the hydrophobic/hydrophilic transition region. The water near the pore surface with the array of SO_3^- groups is called as "surface water" which absorbed by the strong electrostatic attraction of SO_3^- groups. Apart from water, the hydrophilic domain contains only excess protons as mobile species, while the anionic counter charge is immobilized. This is an inherent advantage of such materials over homogeneous electrolytes with mobile anions. Figure 2-8 shows the proton transport mechanisms in various routes.

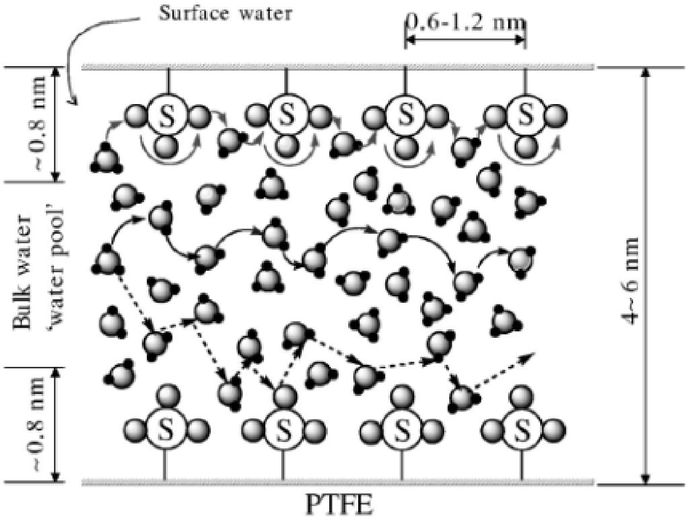

Figure 2-8 Proton transfer in the Nafion in a fully hydrated condition.[3]

2-2-3. Conductivity measurement

Proton conductivity is usually the first property to evaluate when detecting the potential of a new PEM material. The main power of PEMFC comes from the ability of the PEM to transport protons from anode to cathode. There are two common measurements in the direction of thickness, one is 2-probe[25] and the other is 4-probe methods[26] (Figure 2-9), however, two-probe method is normally used because of convenience and results are more suitable. The four-terminal method commonly measures the resistivity of ion conductors with low resistance, due to the reduced interfacial resistance and polarization, thus the four-terminal dc method should not be used for material with frequency-dependent behavior, such as being both an insulator and dielectric, despite the accuracy, the sensitivity, and the stability of the measurement. However, two-terminal method is restrictively applicable to the measurement of resistivity in material of high resistance, as the contribution for resistance of the lead itself is low enough to be neglected in the total resistance. Flexible polymer membranes such as Nafion are well established for measuring the proton conductivity by 4-probe methods, however, more and more proposed novel PEM materials are inorganic or inorganic-organic composites, usually formed in powder or nanoparticles, for which a 4-porbe measurement is more difficult than 2-porbe measurement. Sample arrangement for 2-porbe measurement was prepared by material sandwiched into electrodes consisting of two of gold or platinum. For the measurement cell which the properties of mechanically strong, chemically resistant and electrically insulating is necessary. Gold and platinum are very suitable to make electrical connections which can avoid ionic poisoning of the proton conducting sample more useful than stainless steels.

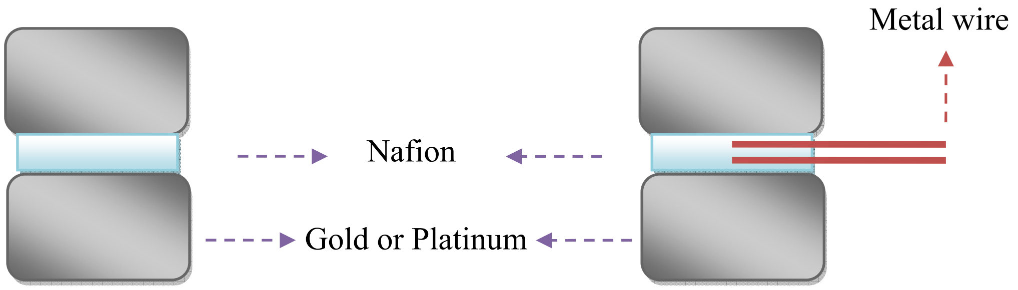

Figure 2-9 Sample arrangements of (a) 2-probe (b) 4-probe measurement in the direction of thickness

The impedance[27], which takes the phase difference into account, is a combined parameter for characterizing an electronic circuit. Its components contained resistors, inductors, capacitors, and the component materials. The definition of impedance (*Z*) is the ratio of the voltage to the current at a given frequency, and it is represented as a complex quantity that consists of a real part (resistance, Z') and an imaginary part (reactance, Z'') with phase angle θ. The equations is described as follow[25]

$$Z' = |Z| \cos\theta$$

$$Z'' = |Z| \sin\theta$$

$$\theta = \tan^{-1}\left(\frac{Z'}{Z''}\right)$$

The impedance can be expressed as $Z' + jZ''$ (Nyquist plot) or as the logarithm of the absolute magnitude of total impedance ($\log|Z|$) vs the logarithm of the angular frequency ($\log\theta$) (Bode plot).

There are several methods for measuring the impedance in practical electrochemical experiments. It depends on the intended use, the magnitude of the impedance, and the measuring conditions. Thus, choosing appropriate method is by considering the frequency range, the measurement range, the measurement accuracy, and the simplicity of operation.

The auto balancing bridge method is commonly used for general purpose measurement in all the ac impedance measurement methods. Its wide frequency range from 5Hz to 40MHz leads its high accuracy over a wide impedance measurement range. Many research have been studied proton conductive materials by measured the impedance and using either the four probe method or the two probe method. Generally, the ionic or electronic conductivity was measured from the resistance of a sample material in dc, to obtain a proton conductivity (σ). Assuming a circuit equivalent, a best-fitting curve was overlaid onto the measurements taken by the 2-probe method which using the two terminals that have the relation between current (I) and voltage (V) across the sample. Conductivity of a sample can be calculated by the formula of $\sigma = (L)/(R \cdot A)$, where that sectional area (A) and length (L) of the samples could be measured. Favorable sample geometry is also important to analysis, the powder material needed to be confined about their dimensions; thickness and cross-section surface area, because these parameters affect the overall accuracy of the proton conductivity measurement. The preparation of powder sample commonly uses pressing the material into a freestanding pellet by a die and a hydraulic press[28]. As testing the ionic conductivity, the materials needed to be saturated with water to make accurate comparisons with Nafion, also the pressed pellets with excess water still maintain their structural integrity without disintegrating. The proton conductivity can be measured in ac impedance spectroscopy and is expressed as the following equation

$$Z = \sqrt{R^2 + (X_c - X_L)^2}$$

$$\theta = \tan^{-1}\left(\frac{X_c - X_L}{R}\right)$$

where X_C and X_L are the capacitive reactance and the inductive reactance, respectively.

The impedance (*Z*) is function of frequency. Thus, the Nyquist plot (Figure 2-10) or the Bode plot are used to show the change in impedance over a reasonable frequency range and gives information on the electrochemical properties of proton-conductive membranes and the interface between the electrodes. Equivalent circuit can be used to describe electrochemical behavior of proton conductive membrane which consist resistors and capacitors. The equivalent circuit for the complex impedance of a Nafion membrane and the electrode structure is shown in Figure 2-11. Each impedance component can be drawn as a hemispheric Nyquist plot and its equation can be described with the real part (Z') and the imaginary part (Z'') over different frequencies, as follow

$$Z=Z'-jZ''=R-j(X_c-X_L)=\frac{R_p}{1+\omega^2C^2R_p^{\ 2}}-j\frac{\omega CR_p}{1+\omega^2C^2R_p^{\ 2}}$$

where R_p and C are the resistance and the capacitance in the parallel circuit, respectively. The ohmic resistance can be obtained from the first approximation of the impedance obtained from the Nyquist plot[29], therefore, the ohmic resistance could be used to calculate the proton conductivity.

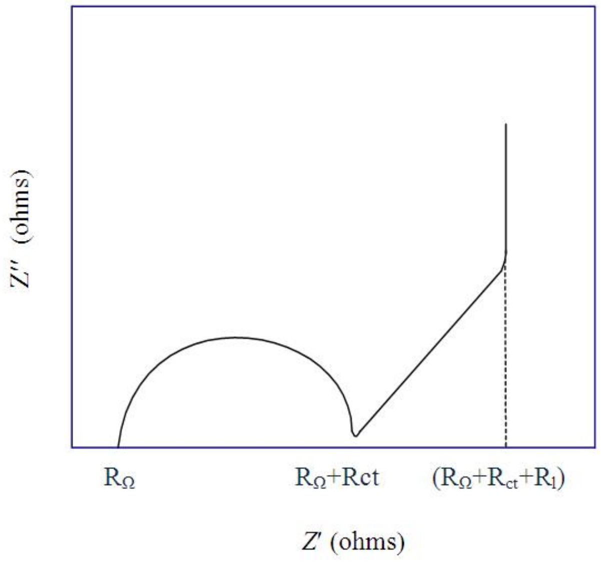

Figure 2-10 The Nyquist plot

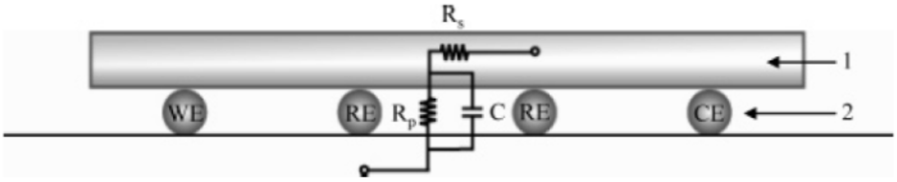

Figure 2-11 The equivalent circuit for the complex impedance of the Nafion membranes and the electrode structure.[25]

2-3. Different kind of proton-conducting materials

Well-known commercial Nafion membranes have been discussed for couple years. It was known that inherently high cost of production, low conductivity at low humidity or high temperature have limited the usages of Nafion, thus numerous researchers have developed new materials to enhance the performance in PEMFCs. Typically, we could separate these membranes for three types, organic, inorganic, organic-inorganic complex. The references regarding organic, inorganic, and complex membranes were summarized in Table 2-2, Table 2-3, and Table 2-4 respectively. There have some studies about improvement of PEMs performance by changing the morphological features, for example, they make these organic materials to be crystal like. In Barique et al. research[30], sulfonated poly (phenylene sulfide) (SPPS) hydrocarbon polymer were presented highly crystalline with outstanding high-temperature stability, good chemical and flame resistances, excellent electrical insulation, antiaging, and precision moldability. In Zhang study[31], 3,4-dimethylbenzaldehyde (DMBA) were used to increase crystallization of Nafion. Nanocrystallites, acting as physical cross-links, play a crucial role in building blocks for improving mechanical durability and stopping fuel crossover. These materials enhance the rate of self-assembly backbones so as to increase the membrane's crystallinity as well as proton conductivity. The possible reason is forming the direct passway for proton transport. In Matsumoto research[32], they mention that proton conducting properties of PEMs basically rely on IECs, water uptake and also ion transport channels which derived from hydrophilic/hydrophobic phase-separated structures. Therefore, they synthesized sulfonated poly (ether sulfone)s which is expected to produce clear phase-separated structures and can induce effective proton conduction. Xu et at.[33] described the synthesis of a new series of aromatic ionomoers with perfluorinated sulfonic acid side chains. It is shown that the perfluorosulfonic acids greatly enhance the proton conductivity of ionomers under high temperature and low humidity conditions. The monomers prepared based on various aromatic ionomers poly(arylene ether) (PAE), poly(ether ether ketone) (PEEK), poly(ether ether sulfone) (PEES) and poly(p-phenylene) backbones with pendant perfluorosulfonic acids. It displayed much higher proton conductivity of 0.107 S/cm, in accordance with its high water uptake and IEC. Yao et al[34], prepared a membrane which was fabricated through incorporating sulfonatd polystyrene (S-PS) electrospun fibers into Nafion. The resultant hybrid membranes had higher proton conductivities (1.8×10^{-1} S/cm) than Nafion, and the conductivities were controlled by selectively adjusting the fiber diameters. Most improvement of organic membranes would like to change the morphology which has long-range ionic pathways to enhance proton conductivity.

In automotive applications, PEMFCs need to be operated under extreme environment even from subzero to high temperature. Thus, PEMs not only have to be very chemical and physical stable but also have good performance under that extreme condition. Proton exists as hydronium ion and migrate (Grotthuss mechanism), therefore water content become a key point for membranes designing. Organic-inorganic composite membranes are designed for trapping water molecules at high temperatures. Ghosh et al.[35], prepared a $MePEG_nSO_3$ acid mixed with a sol-gel based MePEGn polymer. The proton conductivity reached a maximum value of 1.38×10^{-5} S/cm. They also found that the molar equivalent conductivity of the $MePEG_nSO_3H$ acid is correlated with the volume fraction of poly-(ethylene glycol) (PEG) present in their mixture. They suggested that Grotthus mechanism is dominant for proton transportation. Due to the result of that conductivity in these solutions of acid and polymer is a function of the PEG content strongly. Different inorganic fillers or particles of acid which were incorporated in organic membranes are not only for compatible with the chemical and physical limits of the polymer membrane but also for increasing the mobility of proton on its surface and thus the conductivity. Nafion-α-ZrP is one of the examples for organic-inorganic composite membranes. Because of α-ZrP is a Bronsted acid with the ability to donate protons, it traps water molecules and enhances Nafion conductivity at low relative humidity.[36] Another gyroscopic inorganic nanomaterial, such as grapheme oxide (GO), is considered attractive for many applications owing to its unique thermal and mechanical properties. The unique structure and high surface area of the GO may provide more proton transport channels and hold more water, which could be beneficial for the improvement of the proton conductivity and mechanical properties of the membranes. In Zarrin's research[37], a sulfonic acid functionalized graphene oxide Nafion nanocomposite (F-GO/Nafion) has been presented. The proton conductivity of 10 wt % F-GO/Nafion was 0.047 S/cm at 120°C and 30% relative humidity. It is an almost 4-fold improvement for Nafion membrane. Tripathi et al.[38] reported an organic-inorganic nanostructured composite that grafting of aromatic ring and less acidic-COOH groups on chitosan moiety. It was expected to balance its hydrophilic-hydrophobic nature and to enhance proton conducting properties. It was also attached with strong acidic group (-SO_3H) functionalized inorganic for expecting to show high proton conducting properties and stabilities. The proton conductivities was $1.92\text{-}5.31 \times 10^{-2}$ S/cm at ambient temperature dramatically increased at high temperature. Mistry et al.[39] prepared four different hybrid systems which were synthetized by using Nafion 117 and a combination of three silicon and one phosphorus presursors (four different kinds). They chose phytic acid (one of phosphorus presursors) due to its multifunctional structure, so that the hydroxyl groups will allow strong bond formation with water molecules to help retain water at elevated temperature. This hybrid shows conductivities of 0.089 S/cm, similar to that of Nafion at the same conditions.

Most hydrocarbon membranes seem to be unstable by Pt catalysts as PEMFCs work at high-temperature. Because of their oxidation by Pt catalysts and also the tolerance toward CO, the performance of the entire device decrease. To solve these questions, inorganic proton-conducting materials have been investigated as the alternatives. These materials usually are inorganic solid acids which have high proton exchange capability and hydrophilicity. They also are formed as porous a structure and/or are acid functionalized to enhance the water adsorption capacity of the membranes. Marschall et al.[40] used co-condensation synthesis and microwave treatment to prepare the Si-MCM-41, and functionalized the porous SiO_2 with sulfonic acid groups (SO_3H). Not only because pore structures were created to form proton transport channel but also more than one SO_3H group was presented per nm^2 of the inner surface, these materials exhibit a high proton conductivity of up to 0.2 S/cm at 100% relative humidity. The higher pore filling in the samples is helpful for a better guidance of protons through the narrowed pore channels. Moreover, less water is needed to achieve a similar extent of proton transport because the sulfonic acid groups are closer together. McKeen et al.[41] chose zeolite as the proton conducting material to study the influence of hydroxyl groups on proton conductivity. They found that the incorporation of phenyl sulfonic acid groups into hydrophilic nanocrystalline zeolite beta (S-PE-BEA-X) further had high proton conductivity value about 5×10^{-3} S/cm. They suggested that the presence of hydroxyl groups is pivotal in achieving high proton conductivity. It is possible due to the formation of a more complete hydrogen bonded water network in the materials with many dangling -OH, and better water saturation inside the molecular sieves. In Tominaka's study[42], they found that sulfated zirconia had a high conductivity ($> 10^{-2}$ S/cm) value which is even better than that of Nafion. Therefore, they synthesized sulfated zirconia in the form of nanoparticles to be an electrolyte membrane. That modification is considered to be easier to donate proton. Cubic mesostructured aluminosilica with strong acid moieties were prepared by Athens et al.[43]. It exhibited high proton conductivities (ca. 9×10^{-2} S/cm at) at elevated temperatures (120°C). Block-copolymer-directed silica mesophases was formed from strongly acidic solutions, which allow highly ordered cubic mesostructured silica films to be synthesized. After removing the block-copolymer species by calcination, hydrophilic aluminosilica surface moieties can be introduced to the interior mesopore channels under highly alkaline solution conditions, followed by separate covalent grafting of perfluorinated-sulfonic-acid (PFSA) groups from nonaqueous solvents to introduce ion-conducting properties. This synthesis overcomes several severe materials limitations to yield complex materials with robust interconnected channels in films that can sustain proton-conducting properties above 120°C. Another meterals, heteropolyacids (HPAs), are known to be superionic conductors in their fully hydrated states. The highest stability and strongest acidity are the advantages of HPAs. However, the high solubility of HAPs in water limits its application as proton-exchange membranes in fuel cells. Zeng et al.[44] attempted to immobilize HPAs onto mesoporous silica which also has high specific surface area, and nanosized channels. The interconnected internal structure and high structural stability allow their potential applications as proton-exchange membranes operating at elevated temperatures. This material showed the best proton conductivity of 0.07 S/cm at 25 °C.

Table 2-2-2. The references regarding organic membranes.

	Material	Property	Improvement or Proton conductivity	Ref.
1	Sulfonated poly(phenylene sulfide) (SPPS) hydrocarbon polymer	*High-temperature stability *Good chemical and flame resistances *Electrical solation *Anti-aging, and precision moldability	0.1 S/cm at 80 °C	[29]
2	Sulfonated poly(ether sulfone)s	*The large difference in polarity between the densely sulfonated hydrophilic units *The hydrophobic units is expected to produce clear phase-separated structures	Higher than 0.1 S/cm at 80 °C	[31]
3	Crystallized Nafion (assisted by 3,4-dimethylbenzaldehyde DMBA)	* Improving mechanical durability *Stopping fuel crossover	*Big hydrophilic clusters and hydrophobic domains *Mechanical properties, electrochemical performance and proton conductivity were improved.	[30]
4	Aromatic ionomoers with perfluorinated sulfonic acid side chains	*A wide humidity *Low gas permeability *Excellent thermal and chemical stability *Good mechanical properties	0.107 S/cm at 80 °C	[32]
5	Nafion incorporated with sulfonated polystyrene (S-PS) electrospun fibers	*Continuous pathways for facile proton *The conductivities were controlled by selectively adjusting the fiber diameters	1.8×10^{-1} S/cm was observed at 80 °C when the fiber diameter was 0.98 µm.	[33]

Table 2-3 The references regarding organic-inorganic complex membranes.

	Material	Property	Improvement or Proton conductivity	Ref.
1	MePEGn(Tri monomethyl ether, poly monomethyl ether)SO_3H acid and a sol-gel based MePEGn polymer	*Provide coordination sites for small cations *Rapidly reorganize their polymer segments	1.38×10^{-5} S/cm at 55 °C	[34]
2	Zirconium phosphate-Nafion hybrid membranes	*Trap water molecules *Enhance conductivity *Enhance outstanding chemical stability	*These particles could help for water retention at elevated temperature by acting as nanotanks dispersed in the perfluorinated matrix (50-100 nm)	[35]
3	N-p-Carboxy Benzyl Chitosan-Silica-PVA Hybrid Polyelectrolyte	*Mechanically and thermally stable inorganic backbone *High proton conducting properties and stabilities	$1.92\text{-}5.31\times10^{-2}$ S/cm (temperature range from 30 to 70 °C)	[37]
4	Nafion membranes with silica and phosphosilicates	*Improve hydrophilicity *Thermal stability *Mechanical strength *Glass transition temperature *Water retention	0.099 S/cm at 80 °C	[39]
5	Graphene oxide (F-GO) nanosheets fillers in a Nafion	*Thermal and mechanical properties *Provide more proton transport channels *Hold more water	0.047 S/cm at 120 °C	[36]

Table 2-4 The references regarding inorganic membranes.

	Material	Property	Improvement or Proton conductivity	Ref.
1	Si-MCM-41 functionalized with sulfonic acid groups	*Enhance the water adsorption capacity *High thermal stability	0.2 S/cm at at140°C	[39]
2	Sulfonic Acid-Functionalized Zeolite Beta	*High acid strength *Adjustable acid group density *Possibility to block methanol crossover *Increase water retention at high temperature while allowing fast proton transport through the pore space	5×10^{-3} S/cm at120°C	[40]
3	Sulfated zirconia nanoparticles	*As catalyst in fuel cell prototypes *An excellent proton conductor	10^{-2} S/cm at 30 °C	[41]
4	Cubic mesoporouse silica were prepared from strongly acidic solutions and functionalized under highly alkaline conditions, followed by nonaqueous conditions to introduce perfluorosulfonic acid surface groups.	*High surface hydrophilicities *Strong acid functionalities	9×10^{-2} S/cm at120°C	[42]
5	Mesoporous silica nanocomposite functionalized with phosphotungstic acid	*High specific surface area, *Nanosized channels or frameworks with an ordered and interconnected internal structure *High structural stability	0.07 S/cm at 25 °C	[43]

2-4. Key factors to high proton conductivity

2-4-1. Water content

Water content plays an important role in the mechanism of proton transport. Protons not only migrate with water clusters but also diffuse between water molecules. In Peckham research[45], the effects of acid concentration and effective proton mobility upon proton conductivity as well as their relationship to water content was carried out. It has been found that decreasing water content leads to decreasing levels of proton mobility and hence conductivity, presumably due to less screening of the tethered sulfonate groups and hence increasing proton localization. At low RH levels (<70%), it was found that the major factor contributing to different levels of proton conductivity is proton mobility and may reflect differences in the effective use of water under these conditions. To clarify the mechanisms of transport of ions and water molecules in perfluorosulfonated ionomer membranes for fuel cells, the temperature dependence of their transport behaviors was investigated in Saito et al. studied[46] By using three different cations in two types of Flemion membrane, the ionic conductivity, water self-diffusion coefficient (DH_2O), and DSC were measured in the fully hydrated state as a function of temperature. Their result showed that DH_2O in the membranes was found to be influenced by the ratio of freezing and nonfreezing water. DFT calculation of the interaction energy between the cation species and water molecules suggested that the water content and the ratio of freezing and nonfreezing water depend strongly on the cation species penetrated into the membrane. There are some previous works have been examined that proton conductivity to correlate change of the water content with that of conductivity upon hydration/dehydration of Nafion membrane. The dynamics of water and its effect on proton transport kinetics in Nafion membranes at several hydration levels are compared in Moilanen et al. studied[47] They used ultrafast infrared spectroscopy and dilute HOD in H_2O as a probe. From the fluorescence decay of the HPTS protonated state, they found out, at low hydration, no proton transfer occurs because there is very little water in the membrane and what is present is unable to reorient to solvate the proton. As the hydration level increases and the orientational mobility of the water molecules increases, the extent of proton transfer also increases although it never reaches that of HPTS in bulk water. In Kunimatsu[48] research, conductivity change was interpreted in terms of different stated of water based on its vibrational spectra of ATR-FTIR. They found out that the conductivity increases or decreases linearly with the band intensity throughout the hydration/dehydration processes. That may be the first data to correlate the proton conductivity linearly related to water uptake in the membrane. Datta and coworkers[49] used the excited state proton transfer process in the fluorescent probe Coumarin 102 to understand the mobility of cations in the Nafion membrane in a molecular level. They found out that the proton transfer is hindered significantly in these less hydrated Nafion, in other word, that correspond to the decrease in proton conductivity in membranes of lower hydration levels. The hindrance of proton transfer is considered to the more efficient attraction of cationic species by the negatively charged sulfonate groups of Nafion. In the presence of a considerably more amount of water may helpful the movement of the proton.

2-4-2. Surface acidity

As a primary component of PEM fuel cells (PEMFCs), the PEM is required to perform a major function that is acting as an electrical insulator and providing an ionic path for proton transport from anode to cathode. Nafion have achieved the greatest success, because of its nanostructure and water content. Water near the pore surface with SO_3^{2-} groups is referred to as “surface water” and the water in the middle region of the pore is called “bulk water”, however, at low water contents (as the working environment is at high temperature), the interaction among water molecules via hydrogen bonding is low, resulting the primary conductivity providing by the surface water. The proton mobility through the surface is considerable that the strong electrostatic attraction of SO_3^{2-} groups. As the working environment temperature rising, the lower water contents in the PEMs, thus the ability of attracting with proton and water is more and more important in materials. Furthermore, there also have many studies pronounced that more acid site on the surface higher conductivity was obtained[19]. They prepared or functionalized some porous materials with larger surface area which attract with sulfuric acid or phosphoric acid[11] to enhance the conductivity. Marchall et al.[6] prepared the Si-MCM-41 functionalized with sulfonic acid which exhibited a high proton conductivity of up to 0.2 S/cm at 100% relative humidity under continuously rising temperature environment. Because of the sulfonic acid groups are closer together provide a better guidance of protons through the narrowed pore channels even at the less water situation.

Otherwise, the replacement was shown by some materials have less value around -12 of Hammett acidity function H_0[50] which corresponding to 100% sulfuric acid. These kinds of materials with the character as “solid superacids” are very suitable to be a solid electrolyte also provide good proton conductivity. Mostly, porous ceramic films of metal oxides have been the subject of growing interest such as pure metal oxides or binary and ternary mixtures of ZrO_2, TiO_2 or SiO_2 together or with other oxides[51]. It was suggests that the bond between metal and oxygen in hydroxyl group has a covalent bond character because the electronrgativity, thus the O-H bond strength is then weakened and dissociation of H^+ is enhanced. Especially sulfated zirconia, the existence of both Brønsted and Lewis acid sites not only enhance the absorption water ability but also releases more and more H^+ to surrounding environment. More introductions about sulfated zirconia are shown in next section.

2-4-3. Microstructures

Porous structure inorganic materials have several properties that are popularly used as possible solid-state electrolyte alternatives. Their beneficial properties for electrochemical performance include high specific surface area, open channels, and open framework with interconnected internal structure, and chemicals, physicals, and mechanical. However, these materials without any functional groups which have strong attraction with water on the surface, the proton conductivity decrease by the evaporation of water due to the proton conduction just rely on the physisorbed water in the pore. Therefore, the higher adsorption energy of small micropores is aspiration because of the capillarity. The relation between the electrical conductivities and the pore structure were discussed in Nogami et al. research[11] The result showed that the P_2O_5-containing glasses exhibit high conductivities (2×10^{-2} S/cm), even though these glasses have small surface area of pores (1.3 ~ 2.5 nm). Yamada et al.[52] suggested that narrowed pore channels (4~5 nm) may be helpful for proton transport. Through investigation of pore size effect on the proton transfer in porous TiO_2-P_2O_5. Hara et al. Hara et al.[19] examined the property of proton conduct for two different hydrated metal oxide ($SnO_2 \cdot nH_2O$ and $ZrO_2 \cdot nH_2O$) with microstructure. They pronounced that even without the addition of other acids, high proton conductivity still was achieved by the acidity and micropore structure of the $SnO_2 \cdot nH_2O$ surface due to the combined effect of the microstructure and the doping of acids. Moreover, perfluorinated polyelectrolytes like Nafion which consist of a fluorocarbon backbone and sulfonic pendant chain that form a microphase-separated morphology provide the hydrophilic channels for the transportation of proton. Recent work by Yameen and co-workers[53] fabricated silicopoly hybrid membranes and demonstrated that the proton-conducting channels generated from microphase-separated block copolymers architectures created high proton conductivity values around 1×10^{-2} S/cm. Polymer nanocomposites of poly were prepared by Ghosh et al.[33]. This material showed the crystalline nature of the silicate layers which was affected due the nanocomposite formation. They showed that the basal spacings are 1.3 and 2.5 nm and also suggested that the reason for the higher proton conductivity could be due to the nanostructure of organoclays. Since the acid molecules are entrapped inside the gallery through the weak intermolecular interaction with the organoclays, which serve as vehicles for supporting the transportation of protons through the membrane hence the proton conduction increases.

2-5. Sulfated zirconia

2-5-1. Properties of sulfated zirconia

Sulfated zirconia is an anion-modified metal oxide which was passed through by sulfate impregnation by using various sulfating agents; the most commonly used are H_2SO_4 or $(NH_4)_2SO_4$. Some Scientific experiments attributed the high activity of the catalyst[54] to its super acidic properties, i.e., S-ZrO_2 is claimed to be a stronger acid (Figure 2-12) than concentrated sulfuric acid. On the basis of Hammett acidity indicators, suggested that the acidity of S-ZrO_2 exhibits a Hammett acid strength H_0 of -16.03, whereas Nafion® shows only about -12; thus, S-ZrO_2 is recognized as the strongest solid acid[50].

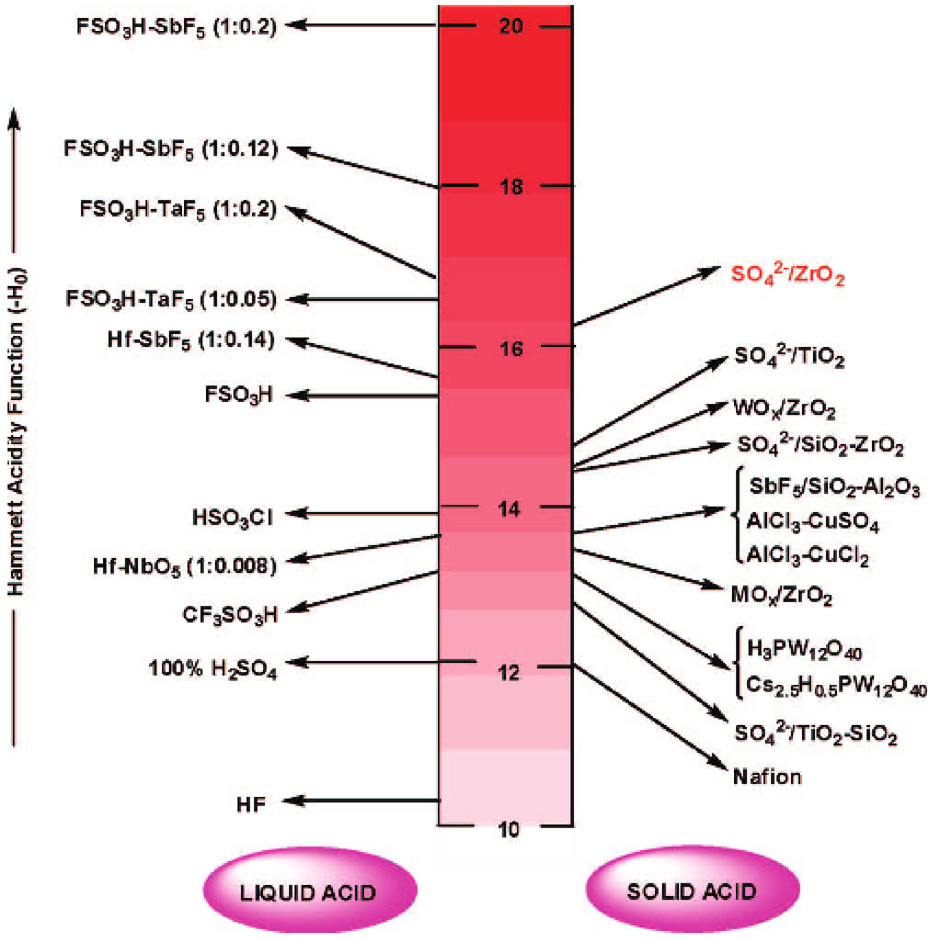

Figure 2-12 Acid strength of various liquid and solid acids.[50]

S-ZrO_2 has been studied extensively in order to elucidate the nature of active sites. A number of studies have attempted to determine the nature of acid sites in the catalyst. There were two sanctifies (Jin et al.[55] and Ward and Ko[50]) suggested similar type of model of S-ZrO_2 by using different kinds of instruments. Jin et al. suggested a structure, in which the sulfate species chelates in to a single Zr atom as presented in Figure 2-13. That the superacid centers are Lewis sites which are associated with the metal cation. The acid strength of this site is enhanced by an electronic induction effect of S=O in the sulfur complex. But for Ward and Ko, in this case a hydroxyl group is bonded to a Zr atom adjacent to the Zr chelated with a sulfate species. Other scientific research suggests that after S-ZrO_2 adsorbed water both

Lewis and Brønsted sites generated are responsible for the proton conducting material. The Brønsted sites are easily interred converted into Lewis sites by evacuation at a temperature above 150 °C. By using diffuse reflectance IR spectroscopy, Kustov et al found that [56] enhanced the strength of both Brønsted and Lewis acid sites.

The presence of protons in the reaction environment is important for the helping transport protons in PEMs. The strong acidity of sulfated zirconia is due to a combination of Lewis and Brønsted acid sites. Along that vein, it was proposed that the highest proton conductivity of S-ZrO_2 is reached.

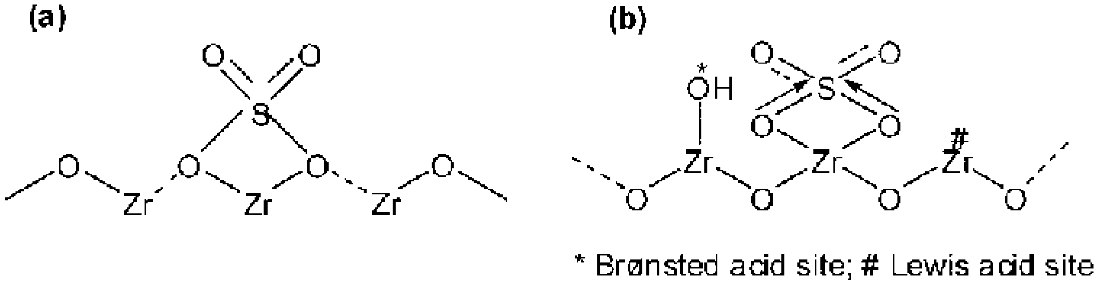

Figure 2-13 Sulfated Zirconia Structure Proposed by (a) Jin et al. and (b) Ward and Ko.[50]

2-6. Porous structure material

2-6-1. Templates

Porous inorganic solids[57, 58] have found great utility as catalysts and sorption media[59] because of their large internal surface area. As this potential application, highly ordered mesoporous inorganic oxides were investigated by the researchers at Mobil Research and Development Corporation in 1992.[17] These materials were prepared by using quaternary ammonium surfactants as a template with negatively charged aluminate silicate; belong to the novel family of so-called M41S aluminosilicate molecular sieves.[17] The scheme is shown in Figure 2-14. The well-defined pores were up to about 3 nm in diameter and also constrained extremely high surface areas (1000 m^2/g). The preparation of the M41S phases represent a new approach in organic-template-assisted synthesis which is called self-assembled molecular aggregates or supramolecular assemblies are employed as the structure-directing agents. The general self-assembly pathway for mesostructured metal oxides is illustrated in Figure 2-15.

Figure 2-14 Different kinds of members of the M41S family.[60]

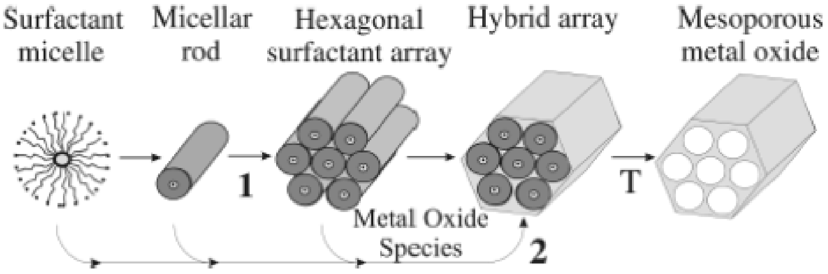

Figure 2-15 Illustration of the synthesis procedure of mesoporous metal oxides possessing a 2D hexagonal pore structure by self-assembly method. [61]

Many different kinds of inorganic mesostructured materials (silica, aluminosilicate, or transition-metal oxides) are obtained by this coprecipitation in an organic liquid crystal mesophase. However, there are so many popular mechanisms established for silica but zirconia, very few studies have been focused on zirconia mesostructured materials. Ciesla et al.[62] and Testaard et al. have proposed a by analogy with silica MCM-41 and have shown the synthesis route respectively. The bridging mechanism was mentioned because of the strong affinity between sulfated and zirconium leads to form polynuclear complexes. The cooperative process between the CTAB hexagonal phase and the polymerization of the inorganic part was proposed in the precipitation of the mesostructured sulfated zirconia phase. Two-step mechanism was proposed: a random nucleation/ growing process and a first –order reorganization form locally ordered cylinders. The schematic drawing of the two-step mechanism is shown in Figure 2-16.

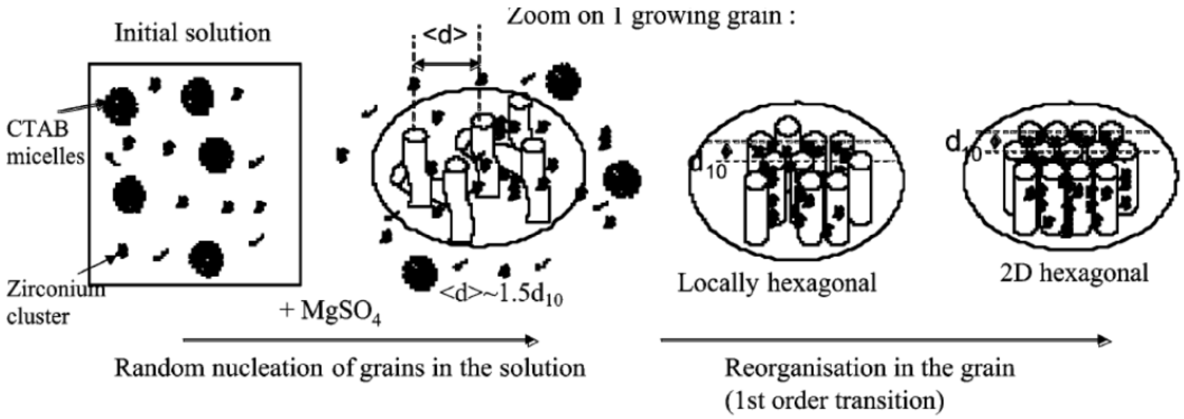

Figure 2-16 The two-step mechanism of the formation of the zirconia/CTAB mesophase.[63]

Chapter 3. Materials and Methods

3-1. Chemicals

Zirconium sulfate tetrahydrate ($Zr(SO_4)_2{\cdot}4H_2O$, Alfa, 98%), hexadecyltrimethyl ammonium bromide (C_{16}TAB, Sigma Aldrich, ≥ 98%) and trimethyl-1-octylammunium bromide (C_8TAB, Alfa, 97%) were used as the precursor and the templates respectively, to prepare porous ZrO_2. Sulfuric acid (H_2SO_4, Showa, 98%) was used for post sulpnation. Ethanol (C_2H_5OH, Echo, 99.5%) and ammonium nitrate (NH_4NO_3, Riedel-de Haën, 98%) were used as an extraction solution to remove the template from the ZrO_2 in terms of ion exchange.

3-2. Preparation of porous sulfated zirconium

Except for S-ZrO_2 sample, which was obtained from calcination of $Zr(SO_4)_2{\cdot}4H_2O$ at 750 °C for 5 hours. Besides, the other samples will be discussed in section 3-2-1 and 3-2-2.

3-2-1. Precipitation process

The surfactant (C_{16}TAB, 1.47g) was dissolved in water (50ml), and $Zr(SO_4)_2{\cdot}4H_2O$ (2.68g) was dissolved in water (14.7 ml) was added. This led to a white precipitate. The molar ratio of the individual components of CTAB to Zr was 0.50. The mixture was stirred for 2h at room temperature and then heated at 100 °C for 1 day in a closed beaker with Teflon covering. After filtration, the precipitate was calcined at 500 °C for 5 hours. This product was called C_{16}S-ZrO_2. A serious molar ratio (0.25, 0.38, and 0.63) by changing the mass of surfactant was prepared also.

The sample C_{16}S-ZrO_2 which molar ratio is 0.5 (0.5g) was added to different concentration sulfuric acid solutions (0.3, 0.6, 0.9 and 1.2 M) for further coating. The mixture was stirred at room temperature for 2 hours. After pumping, the powders were calcined at 500 °C for 5 hours once again.

3-2-2. Hydrothermal process

The surfactant (C_8TAB, 1.9g) was dissolved in water (35ml), and $Zr(SO_4)_2·4H_2O$ (2.68g) was dissolved in water (14.7 ml) was added. The molar ratio of the individual components of C_8TAB to Zr was 0.50. The mixture was stirred for 2h at room temperature and then under hydrothermal processing at 150°C for 36 hours. This process led to a white precipitate. To remove the surfactant efficiently, the precipitant was filtered and extracted with 150 ml alcoholic solutions (99%) and this product was called C_8S-ZrO_2 (EtOH). Another one which was filtered and extracted with alcoholic solutions with ammonium nitrate (150 ml of ethanol containing 1.6 g of NH_4NO_3) was called C_8 S-ZrO_2 (IEE). Both of them were under stirred condition at 60°C for 15 mins for three times. The amount of NH_4NO_3 corresponded to $NH_4^+/CTAB^+$ molar ratio is 2. The extracted sample after filtration was calcinated at 500°C for 5 hours.

3-3. Characterization

3-3-1. Nitrogen adsorption and desorption isothermal

The specific surface area, S_{BET}, and pore sizes were determined from Brunaner, Emmett and Teller model (BET) and Barrett, Joyner and Halenda formula (BJH), respectively. This is based on the N_2 adsorption and desorption isothermal at 77K by Micromeritics, Tristar 3000. Prior to the adsorption/desorption, the samples were degassed at 150°C under vacuum for 12 hours.

3-3-2. Fourier Transform Infrared Spectrometer (FTIR)

The S-ZrO_2 samples were identified using Fourier transform infrared spectrometer (FTIR, Thermo Scientific Nicolet iS10) scan from 400 to 4000 cm^{-1} with the resolution of 4 cm^{-1} for 100 cycles. The samples were mixed with KBr (Merck) and then pressed as a flake for the FTIR measurement.

3-3-3. X-ray photoelectron Spectroscopy (XPS)

The surface chemical compositions and chemical states of the S-ZrO_2 samples were characterized using X-ray photoelectron spectroscopy (XPS, ESCA PHI 1600) using an Al Kα X-ray source (1486.6 eV). The photoelectron was collected into the analyzer with pass energy of 23.5 eV. In the collection step, size in wide range scan and high-resolution analysis were 0.1 eV. All analytical process was controlled under ultrahigh vacuum conditions at pressure less than 1.4×10^{-9} Torr. The chemical shift in binding energy of XPS spectra was reference to the Zr (3d) line at 182.4 eV. In order to quantify and qualify each element, curve fitting of the XPS spectra was performed. After subtraction of the "Shirley-shaped" background, the original spectra were fitted using a nonlinear least-square fitting program and combination of Gaussian-Lorentzian peak shapes were adapted for all peaks. The parameters used for the curve fitting of the Zr 3d, S 2p, O 1s, C 1s, including the binding energies, doublet separation, and full-width at half maximum. The integrated peak areas were normalized atomic sensitive factors to calculate atomic ratios.

The equation for atomic ratio calculation is shown below,

$$n_1/n_2 = (I_1/ASF_1)/(I_2/ASF_2) = (A_1/ASF_1)/(A_2/ASF_2) \qquad (3\text{-}1)$$

where as,

n: atomic number

I: intensity of XPS spectra

ASF: atomic sensitivity factor

A: peak area of XPS spectra

3-3-4. Thermo Gravimetric Analysis (TGA)

The organic volume and energy flow of the samples were measured using thermo gravimetric analysis (TGA, TA5100). The samples were heated from room temperature to 900°C at a heating rate of 10°C/min under an air flow with a flow rate of 50 ml/min.

3-3-5. Water content measurement

Water contents were measured using thermal gravimetric analysis (Perkin Elmer SII, pyris diamond TG/DTA analyzer). The sulfated ZrO_2 powders (0.08g) were pressed into pellets with 1.2 cm in diameter and 25 mm in thickness at 1960 kPa. A 0.05 ml of water droplets was added to the pellet to wet the samples. Samples were pat-dried with tissue paper to remove the surface water. Samples were heated from room temperature to 400 °C at 10 °C min^{-1} under N_2 flow with 10 ml min^{-1}. The weight of dry membranes was determined from the point at which degradation of sulfonic acid begins (400 °C). Water content was calculated according to the follow equation

$$\text{Water content} = \frac{\text{weight of wet pellet - weight of dry pellet}}{\text{weight of wet pellet}} \times 100\%$$

3-3-6. Proton conductivity measurement

For 2-probe measurements in the direction of thickness, specimens were prepared by specimen sandwiched into electrodes consisting of two pieces of gold sheets situated opposite each other. A specimen fixed to a measuring cell was placed inside a temperature and humidity chamber under constant temperature and humidity (Room temperature, 100%RH). AC impedance (PGSTAT 30) measurements were taken using a computer-controlled Autolab model, and Cole-Cole (Z’-Z”) plots were obtained. The frequency limits of the sinusoidal signals were typically set between 100Hz and 10000Hz, with an oscillation of 100 mA. A best-fitting curve was overlaid onto the measurements taken by the 2-probe method. The sulfated ZrO_2 powders were pressed into pellets with 1.2 cm in diameter and 25 mm in thickness at 1960 kPa. In contrast to Nafion117, the membrane was cut with 1.2cm in diameter and 20 mm in thickness. A 0.05 ml of water droplets was added to the pellet and Nafion117 to wet the samples. The pellet was sandwiched into electrodes consisting of two pieces of gold sheets situated opposite each other. A specimen fixed to a measuring cell was placed inside a temperature and humidity chamber under constant temperature and humidity (Room temperature, 100% RH). The frequency limits of the sinusoidal signals were typically set between 100Hz and 10000Hz, with an oscillation of 100 mA. Conductivity was calculated from the obtained membrane resistance, R_{bulk}, by using the following formula.

$$\sigma = L/(R\cdot A) \qquad (3\text{-}2)$$

Where

σ is conductivity (Scm^{-1}),

L is membrane thickness (cm),

A is an electrode area (cm^2) and

R is resistance (Ω).

3-3-7. Temperature programmed desorption (TPD)

The TPD (Auto Chem II 2920) experiments were used to measure the acidity by using probe of ammonia. The samples (0.10-0.15 g) were pretreated in He for 1 h at 200°C and then cooled to 100°C. At this temperature, NH_3 was pulsed over the samples and adsorbed for 1hr. The physically adsorbed NH_3 was desorbed in He at a rate of 25ml min^{-1} for 30 min. Desorption was programmed form 100 to 600°C at a heating rate of 10°C min^{-1}. A thermal conductivity detector (TCD) was used to monitor the desorption volume of NH_3.

3-3-8. High Resolution Transmission Electron Microscope (TEM)

The particle size and shape of nanocrystals were examined by a high resolution transmission electronic microscopy (HR-TEM, JEOL JEM-2010) at an accelerating voltage of 200 KV. The specimen was prepared by dispersing of powders into acetone with ultrasonic vibration. The colloid was dropped on a holey carbon film supported on a Cu grid (Ted Pella, Inc., 200 meshes).

3-3-9. Inductively Coupled Plasma- Mass Spectrometry (ICP-MS)

ICP-MS (Perkin Elmer, SCIEX ELAM 5000) was used to analyze bulk chemical compositions including S/Zr ratio of samples. All solid samples were digested with acid solution coupled with microwave.

Chapter 4. Result and Discussion

4-1. Thermal Analysis

To understand the thermal behaviors of samples obtained from different preparation methods and the molecular fragments released during the calcination process, thermogravimetric analysis (TGA) curves were examined. Figure 4-1 shows the TGA curves of $Zr(SO_4)_2 \cdot 4H_2O$ and the as-prepared $C_{16}S$-ZrO_2, C_8S-ZrO_2, and the C_8S-ZrO_2 (IEE). The $Zr(SO_4)_2 \cdot 4H_2O$ exhibited three weight-loss stages, in which the weight losses in the temperature ranges of 25-120 °C and 120-200 °C are associated with the removal of adsorbed and bound water, respectively. A significant weight loss of 36 % in the range of 525-695 °C is due to the decomposition of sulfated species. In addition to the elimination of adsorbed water below 200 °C, the as-prepared $C_{16}S$-ZrO_2 sample had a weight loss of 31 % between 200 and 500 °C, corresponding to the oxidation of the surfactant. A small weight loss of 7 %, resulting from the decomposition of sulfated residues, took place in the range of 500-560 °C. Similar phenomenon was observed in the as-prepared C_8S-ZrO_2 sample. Moreover, ion exchange treatment with NH_4NO_3/C_2H_5OH solution greatly removed the organic template from the C_8S-ZrO_2 sample. Remaining water and the template only contributed 2 and 4 %, respectively, to the total mass of the sample. It is noted that the temperature for the elimination of sulfated species (3 % weight loss) occurred at 700-760 °C. The temperature was higher than those of the similar process in the other samples, inferring that different sulfated species resulted from the ion-exchange-treatment.

$$\left\{Zr(OH)_4, SO_4^{2-}, CTAB^+\right\} \xrightarrow{NH_4^-} \left\{Zr(OH)_4, SO_4^{2-}, NH_4^-\right\} \xrightarrow{\Delta} \left\{ZrO_2, SO_4^{2-}\right\}$$

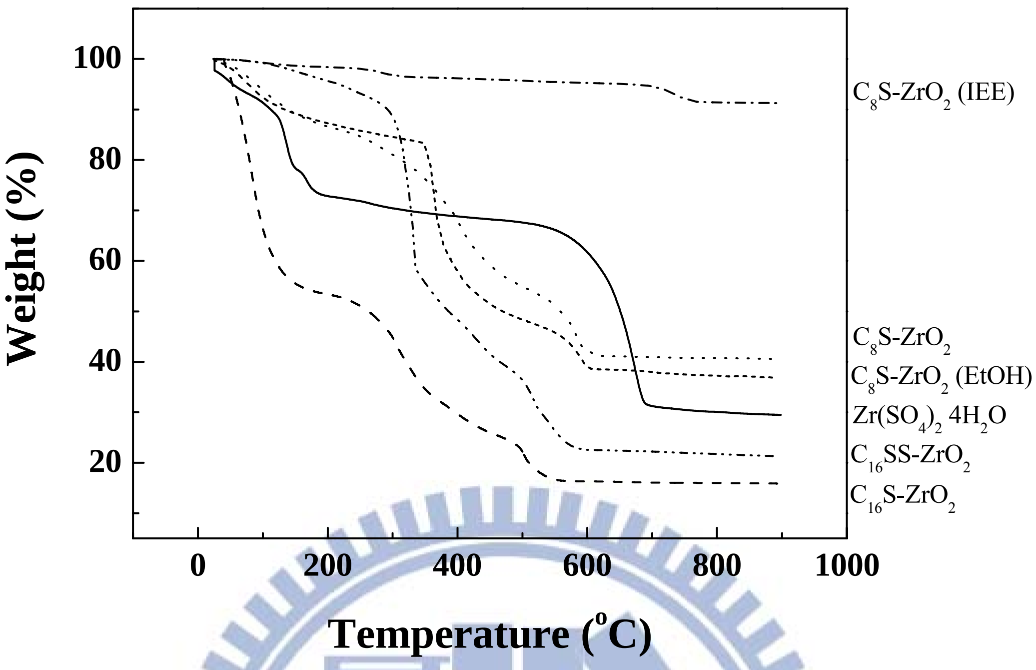

Figure 4-1 The TGA curve of $Zr(SO_4)_2 \cdot 4H_2O$, and as-prepared $C_{16}S$-ZrO_2, $C_{16}S$-ZrO_2, C_8S-ZrO_2, C_8S-ZrO_2 (EtOH) and C_8S-ZrO_2 (IEE).

In this study, the surfactant molecules in the $C_{16}S$-ZrO_2 and C_8S-ZrO_2 samples were removed thorough calcination at 500 °C for 5 hr. In addition, the S-ZrO_2 sample was obtained from calcination of $Zr(SO_4)_2 \cdot 4H_2O$ at 750 °C for 5 hr. To determine the quantity of the sulfated species remaining in the $C_{16}S$-ZrO_2, C_8S-ZrO_2, and S-ZrO_2 samples, their TGA curves were recorded and shown in Figure 4-2. The S-ZrO_2 sample exhibited little mass loss in the range of 25-900 °C, indicating that the calcination at 750 °C effectively eliminated sulfated species from the $Zr(SO_4)_2 \cdot 4H_2O$. This finding is in agreement with the TGA result of the $Zr(SO_4)_2 \cdot 4H_2O$ sample that sulfated species was completely removed above 750 °C. The $C_{16}S$-ZrO_2 and C_8S-ZrO_2 samples started to undergo 4 and 8 % weight loss at 590 and 690 °C, respectively. The weight losses represent the amounts of the sulfated species remained in these two samples because the calcination temperature (500 °C) was lower than the temperatures (570-620 °C) required for entirely removing the sulfated species from the samples. In fact, S elements were also identified in the samples from XPS and ICP-MS. These results indicate that sulfated zirconia powders were successfully obtained through the preparation processes in this study. The $C_{16}S\text{-}ZrO_2$ sample contained about 4 % mass from adsorbed water. In contrast, only few amounts of water were present in the $C_8S\text{-}ZrO_2$ sample. The difference in the water contain in these two porous samples is attributed to their different pore sizes.

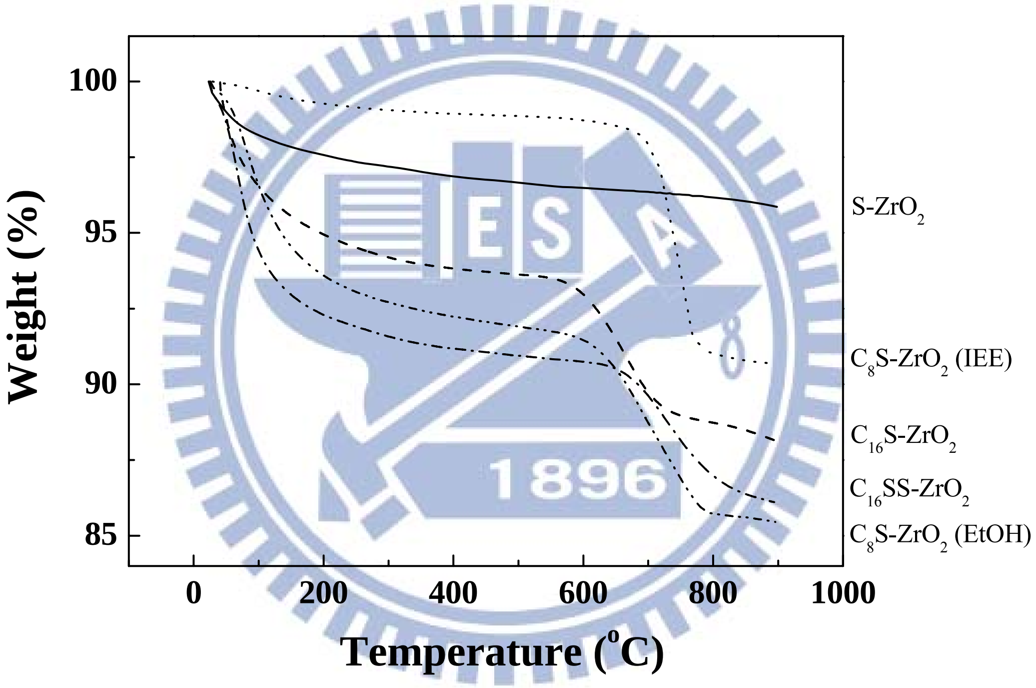

Figure 4-2 The TGA curves of $C_{16}S\text{-}ZrO_2$, $C_{16}SS\text{-}ZrO_2$, $C_8S\text{-}ZrO_2$(IEE), $C_8S\text{-}ZrO_2$(EtOH), and $S\text{-}ZrO_2$ samples.

4-2. Surface functional group

Figure 4-3 shows the FTIR spectra of S-ZrO_2, C_{16}S-ZrO_2, C_{16}SS-ZrO_2, C_8S-ZrO_2 (IEE), and C_8S-ZrO_2(EtOH) samples. Intensive Zr-O absorptions in the region of 400-800 cm^{-1} indicate that calcination turned all the samples into ZrO_2 forms[54]. In addition, almost hydrocarbons were burned out from the templated C_{16}S-ZrO_2, C_{16}SS-ZrO_2, C_8S-ZrO_2 (IEE), and C_8S-ZrO_2(EtOH) samples after the thermal treatment at 500 °C because the C-H absorptions were absence in their IR spectra. Except for the S-ZrO_2 sample, all the templated ZrO_2 powders showed the significant S-O and S=O stretching absorptions in the region of 850-1450 cm^{-1}.[64] The C_{16}S-ZrO_2, C_{16}SS-ZrO_2, and C_8S-ZrO_2(EtOH) samples contained the S=O symmetric stretching absorption at 1270 cm^{-1}. In addition, the S-O asymmetric stretching bands at 1220, 1140, 1070, 991 cm^{-1} were observed, revealing that SO_4 species bidentately complexes to the ZrO_2 matrix.[54] The C_8S-ZrO_2 (IEE) sample showed a different sulfated absorption feature. The S-O absorption at 1140 cm^{-1} became the most intensive in the SO_4 absorption set. In addition, the S=O stretching mode blue shifted to 1345 cm^{-1}.[64] These phenomena suggest a polysulfated species.

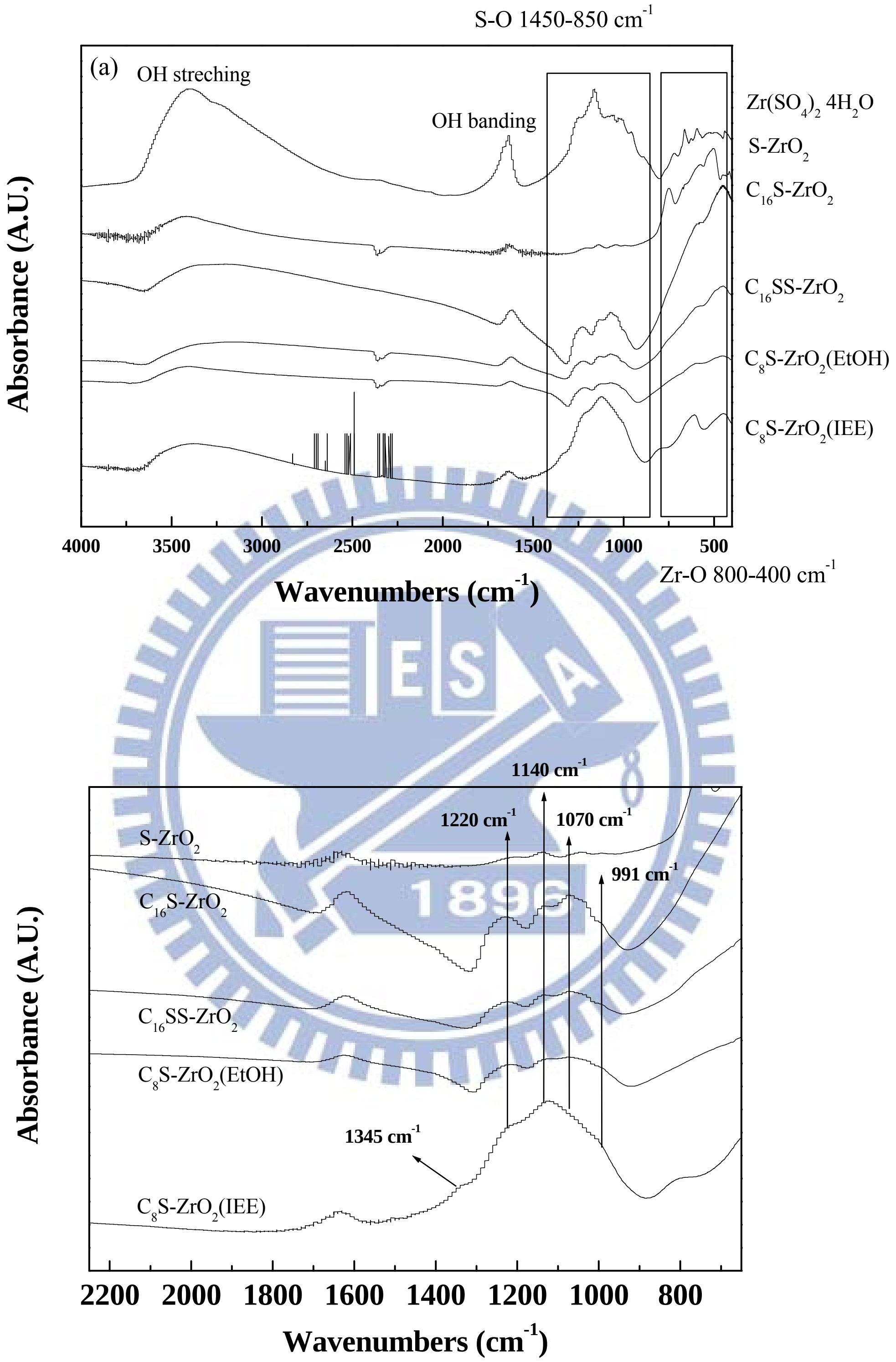

Figure 4-3 FTIR spectra of the S-ZrO_2, C_{16}S- S-ZrO_2, C_{16}SS- S-ZrO_2, C_8S- S-ZrO_2 (IEE), and C_8S-ZrO_2 (EtOH) samples. (a) the original spectra, and (b) the zoom-in spectra in the 700-2200 cm-1.

4-3. Chemical compositions

The quantities and bonding of the sulfated species on the surface of the ZrO_2 samples determine proton-transfer efficiency. To understand the surface properties of the sulfated ZrO_2 powders, all the samples were characterized by using XPS and ICP-MS. Figure 4-4 shows the S (2p) XP spectra of the S-ZrO_2, C_{16}S-ZrO_2, C_{16}SS-ZrO_2, C_8S-ZrO_2 (IEE), and C_8S-ZrO_2(EtOH) samples. Theoretically, the S (2p) photoelectron line appears in the binding energy of 168.5-171.3 eV.[65] However, the S (2p) peak in the ZrO_2 matrix in this study was significantly interfered with other photoelectron lines. After deconvolution, there were four peaks contained in the broad signal ranging from 166 to 177 eV. Similar phenomenon was observed in Marcus's[65] and Milburn's[66] research. To ascertain the S (2p) peak from the interferences, three samples including pure ZrO_2, sulfuric-acid soaked ZrO_2 and TiO_2 powders were additionally prepared. The pure ZrO_2 powders showed the broad peak in the range of 168-177 eV (see Appendix A-1). After soaking with sulfuric acid, the ZrO_2 sample exhibited an additional peak centered at 168.64 eV. Moreover, the soaked TiO_2 sample showed the single peak at 169.0 eV. These results clearly evidence that the deconvoluted peaks centered at 168.64-169.0 eV belong to S (2p) photoelectron line, and the other peaks at higher binding energies arise from ZrO_2 matrix effect. All the sulfated samples exhibited one S (2p) photoelectron peak except for the C_8S-ZrO_2 (IEE) sample. In addition to the S (2p) peak at 168.2 eV, the C_8S-ZrO_2 (IEE) sample had another S (2p) peak at 169.4 eV, which is attributed to poly-sulfated species.

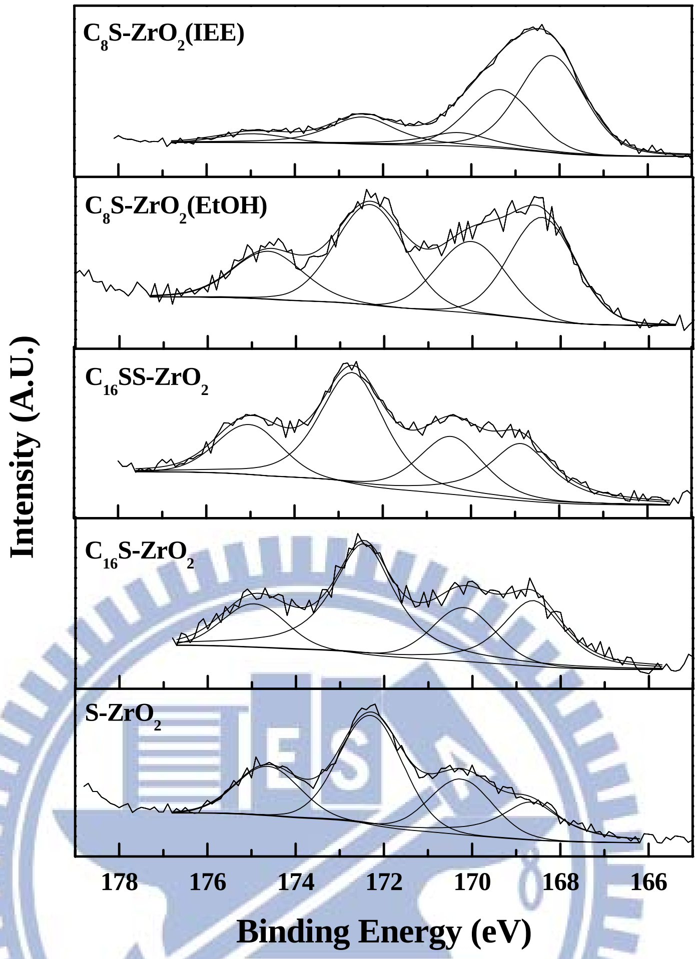

Figure 4-4 The S (2p) XPS of the S-ZrO_2, C_{16}S-ZrO_2, C_{16}SS-ZrO_2, C_8S-ZrO_2 (EtOH), and C_8S-ZrO_2 (IEE) samples.

The surface and total S/Zr atomic ratios of the sulfated ZrO_2 samples are summarized in Table 4-1. Calcination of $Zr(SO_4)_2$•$4H_2O$ at 750 °C removed most of sulfated ions from the S-ZrO_2 sample. However, the XPS results showed 0.1 of S/Zr ratio on its surface, indicating that the remaining sulfated species is primarily incorporated in the surface layer. The C_{16}S-ZrO_2 and C_{16}SS-ZrO_2 samples had similar bulk and surface S/Zr ratios of 1.9×10^{-2}-2.1×10^{-2} and 0.15-0.18, respectively. Addition of sulfuric acid in the precipitation process only assists the formation of regular pore sizes, but has little effect on the surface composition. The C_8S-ZrO_2 (EtOH) powders had the bulk and the surface S/Zr ratios of

20.3×10^{-2} and 0.38, respectively. These values are larger than the S/Zr ratios of the mesoporous samples. Because the C_8S-ZrO_2 (EtOH) sample had microporous structure, the micropore confinement presumably inhibits S-O-Zr bond vibrations and breaking. The C_8-S-ZrO_2 (IEE) sample exhibited the highest S/Zr ratios both in the bulk (94.8×10^{-2}) and at the surface (1.02). Replacement of octylammonium ions with NH_4^+ though ion exchange treatment enhanced the stability of sulfated species against thermal treatment. This result is in agreement with its TGA curve which shows the higher temperature for removal of the sulfated species. We further compared the surface and the bulk S/Zr ratios and found that the surface ratios were 10, 7, and 2 times higher than the bulk ratios in the $C_{16}S$-ZrO_2, $C_{16}SS$-ZrO_2, C_8S-ZrO_2 (EtOH) samples, respectively. Like the S-ZrO_2 sample, this finding indicates that the sulfated species was mainly incorporated on the surface. The C_8S-ZrO_2 (IEE) sample showed similar surface and bulk S/Zr ratios, revealing the bulk doping.

Table 4-1 Sulfur-to-zirconium atomic ratios in the different sulfated ZrO_2 samples.

	S/Zr atomic ratio	
Samples	ICP-MS	XPS
S-ZrO_2	-[a]	0.10
$C_{16}S$-ZrO_2	1.9×10^{-2}	0.18
$C_{16}SS$-ZrO_2	2.1×10^{-2}	0.15
C_8S-ZrO_2 (EtOH)	20.3×10^{-2}	0.38
C_8S-ZrO_2 (IEE)	94.8×10^{-2}	1.02

a- represents unavailable.

Figure 4-5 shows the O (1s) XP spectra of the sulfated ZrO_2 samples. The O (1s) peak in all the sulfated samples can be fitted into O-Zr (BE= 530.0 eV), O-S (BE= 531.6 eV) and O-H (532.6 eV) states.[67] To derive the sulfated species and surface chemical structure of the sulfated samples, the O-S/S, O-Zr/Zr, and O-H/Zr atomic ratios were calculated and listed in Table 4-2. The S-ZrO_2 sample had the O-S/S ratio of 3.89, suggesting 4-coordinated S elements. The three templated samples, including C_{16}S-ZrO_2, C_{16}SS-ZrO_2, and C_8S-ZrO_2 (EtOH), showed the S-O/S ratios in the range of 3.54-3.66, revealing a pyrosulfate species ($S_2O_7^{2-}$). A low S-O/S ratio of 3.10 was found in the C_8S-ZrO_2 (IEE) sample. Polysulfated species was considered to be formed at the ZrO_2 sample.[68] In addition, bulk doping resulted the C_8S-ZrO_2 (IEE) sample in a non-stochiometric Zr-O/Zr ratio of 1.44 and a high O-H/Zr ratio of 0.29. These features imply its higher surface Lewis and Bronsted acidity over the other samples.

Table 4-2 The surface O-S/S, O-Zr/Zr, and O-H/Zr atomic ratios

Samples	O-S/S	(O-Zr)/Zr	O-H/Zr
S-ZrO_2	3.89	1.77	0.18
C_{16}S-ZrO_2	3.54	2.39	0.20
C_{16}SS-ZrO_2	3.66	2.01	0.14
C_8S-ZrO_2 (EtOH)	3.60	1.95	0.20
C_8S-ZrO_2 (IEE)	3.10	1.44	0.29

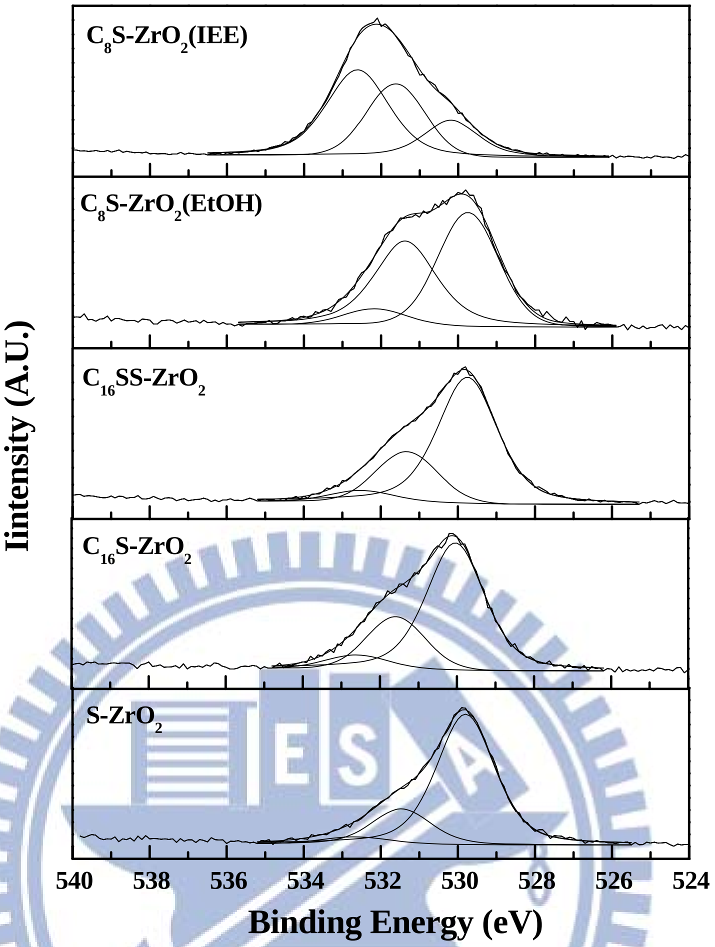

Figure 4-5 The O (1s) XPS of the S-ZrO_2, C_{16}S-ZrO_2, C_{16}SS-ZrO_2, C_8S-ZrO_2 (EtOH), and C_8S-ZrO_2 (IEE) samples.

According to the XPS and FTIR results, we propose the different chemical structures of sulfated species on the ZrO_2 surface. The sulfated group (SO_4) monodentately or bidentately bonds to the Zr^{4+} ions on the surface of the S-ZrO_2 sample. Its oxygen deficient property (O-Zr/Zr= 1.77) infers to the Lewis acidity. Templating methods lead pyrosulfated groups bidentately binding to the ZrO_2 surface. Poly-sulfated moieties are introduced into the ZrO_2 surface lattice after the ion exchange treatment.

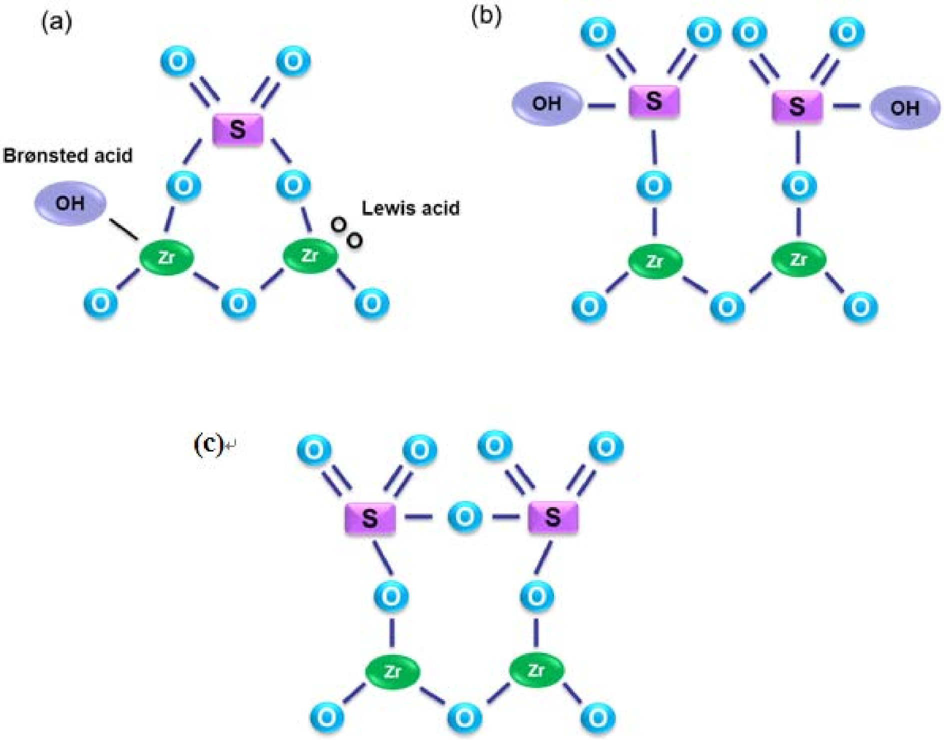

Figure 4-6 The chemical structures of the sulfated groups on the different ZrO_2 samples. (a) the S-ZrO_2 powder, (b) the C_{16}S-ZrO_2, C_{16}SS-ZrO_2, and C_8S-ZrO_2 (EtOH) samples, (c) the C_8S-ZrO_2 (IEE) sample.

Through extraction of MCM-41 materials with an ethanolic ammonium nitrate solution, Lang and Tuel[69] efficiently remove the organic template from the templated samples. The exchange of the organic cations with the NH_4^+ ions preserved the porous structure and led to the porous structure similar to those obtained after calcination. In this study, we used the similar procedure to remove the C_8TAB from the ZrO_2 sample before calcination to prevent incomplete oxidation during the thermal treatment. However, the microporous structure was destroyed by the ion exchange treatment. This result is attributed to the dehydration of the sample induced by the high ionic strength of the salt solution. The dehydration shrinks the micropores, thus causing the disappearance of the pores in the following calcination. The sulfated species on the pore wall surface was incorporated into the ZrO_2 matrix through the elemental rearrangement, and some of them were segregated from the lattice to the particle surface due to the limitation of solubility. A high concentration of the surface sulfated species formed polysulfated moiety.

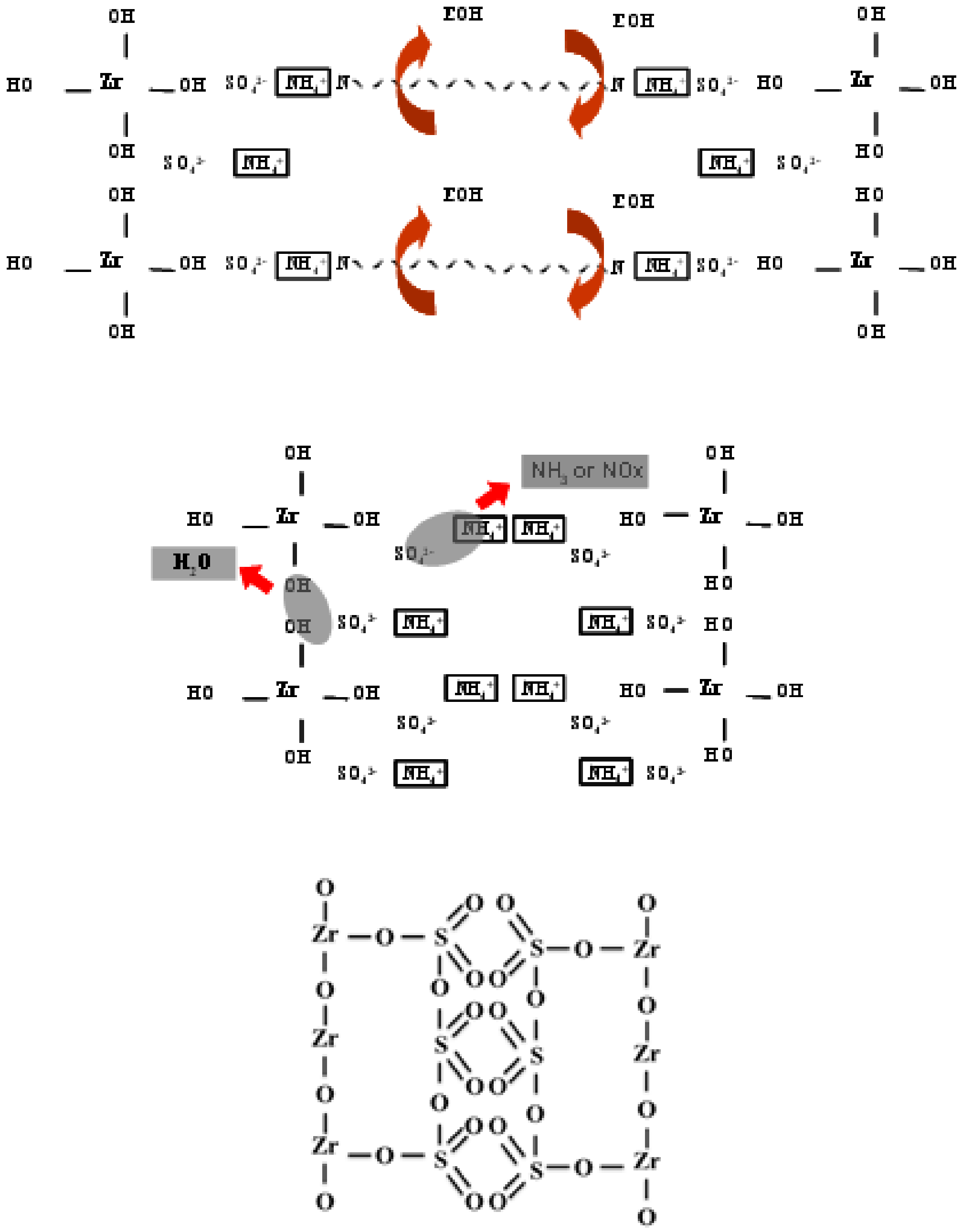

Figure 4-7 Formation of C8S-ZrO2 (IEE).

4-4. NH_3 adsorption and desorption

To examine the surface acidity of the sulfated samples, their TPD measurements were carried out, and the results are shown in Figure 4-8. The S-ZrO_2 sample showed a desorption peak at 235 °C, which is devoted to the adsorption at the Lewis acid sites with medium strength. Substantial amounts of medium Lewis acid and strong Bronsted acid sites were found in the C_8S-ZrO_2 (IEE) sample at 290 and 510 °C, respectively. Its low O-Zr/Zr and high O-H/Zr ratios support the TPD result. The C_{16}S-ZrO_2, C_{16}SS-ZrO_2, and C_8S-ZrO_2 (EtOH) had intensive desorption peaks at 176-188 °C, which is ascribed to the NH_3 adsorbed on weak Lewis acid sites.[70]

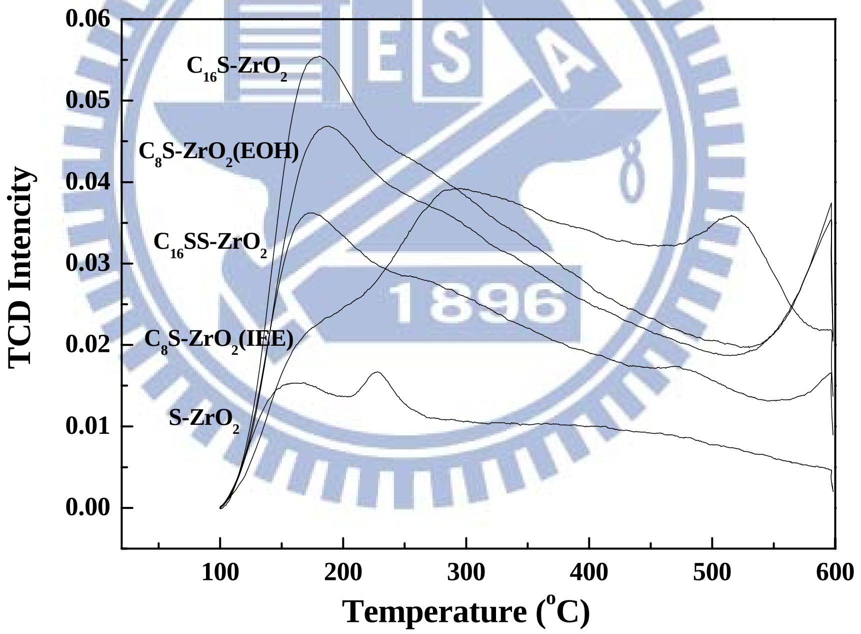

Figure 4-8 NH_3 TPD patterns of the S-ZrO_2, C_{16}S-ZrO_2, C_{16}SS-ZrO_2, C_8S-ZrO_2 (EtOH), and C_8-S-ZrO_2 (IEE) samples.

4-5. Textures and proton conductivities of the sulfated zirconia

To explore the effect of porous structures on the proton conductive capability, the textures of the sulfated samples were characterized in terms of N_2 physisorption at 77 K. The S-ZrO_2 sample (Appendix B-1) showed a Type IV adsorption isotherm[71] and a H3 hysteresis loop.[72] The mesoporous feature resulted from its interparticle voids. Without templating effect, the sample had a small surface area of 64 m^2/g and relatively large pore size of 16.4 nm. In addition to the C_{16}S-ZrO_2 sample that was prepared with the CTAB/Zr molar ratio of 0.5, the samples with the CTAB/Zr ratios of 0.25, 0.38, and 0.63 were also prepared. Figure 4-9 and Figure 4-10 show the N_2 adsorption/desorption isotherms and pore size distributions of the C_{16}S-ZrO_2 samples prepared with different CTAB/Zr molar ratios. Typical Type IV adsorption isotherms were observed in the C_{16}S-ZrO_2 samples when the CTAB/Zr ratio was higher than 0.50, indicating mesoporous structures. In addition, the hysteresis loop (H2 or H3) was observed in the relative pressure range from 0.4 to 0.8. The inflection was not sharp, indicated that the pores are not a uniform size and has broad distribution. The gentle inflection reveals wide pore-size distributions. All these C_{16}TAB-templated samples exhibited continuous increase in the pore volume when the pore size was smaller than 4.4 nm. Moreover, higher amounts of the template resulted in larger numbers of the meso/micro pores. The samples with the CTAB/Zr ratios higher than 0.5 showed a typical pore size of 3.9 nm, which is resulted from self-assembled micelles.

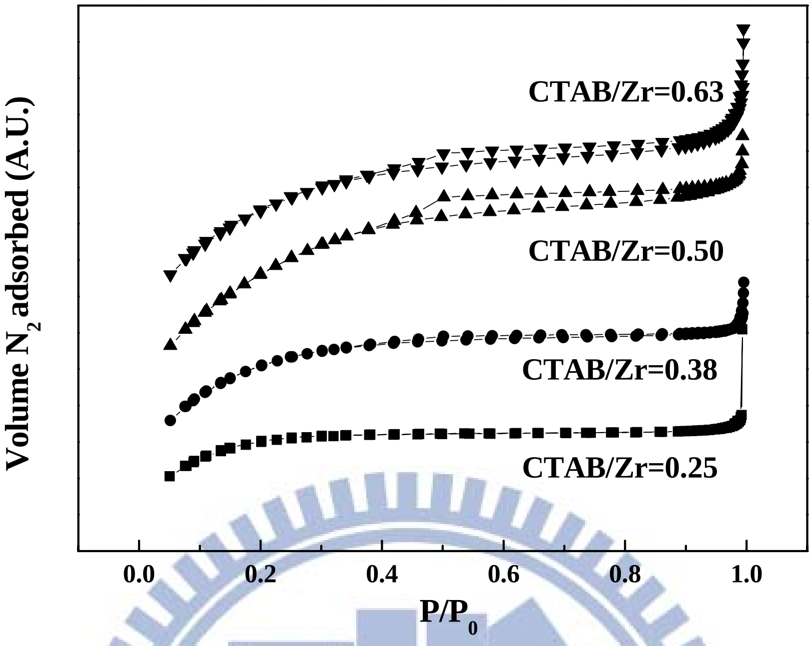

Figure 4-9 Nitrogen adsorption-desorption isotherms of the $C_{16}S$-ZrO_2 samples synthesized with different CTAB/Zr molar ratios.

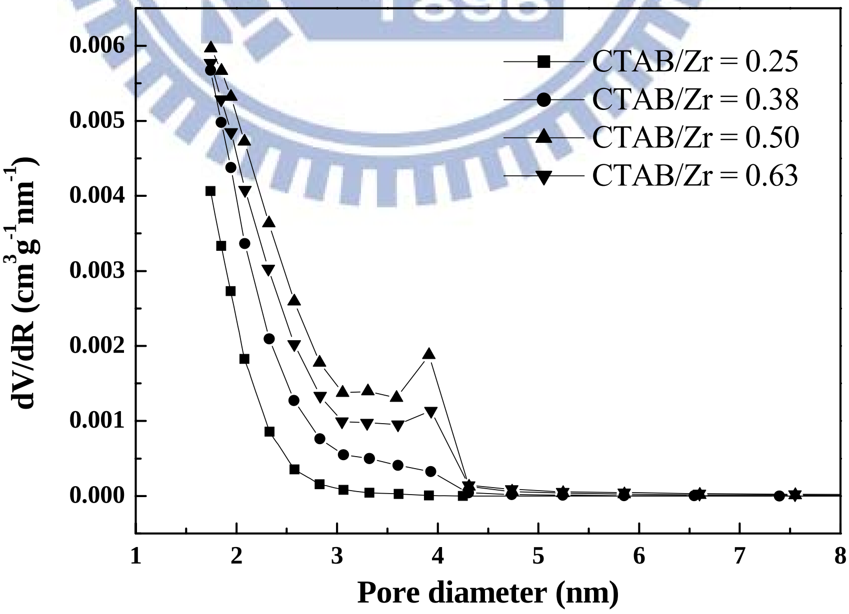

Figure 4-10 Pore size distributions of the $C_{16}S$-ZrO_2 samples synthesized with different CTAB/Zr molar ratios.

Table 4-3 summarizes the surface areas, pore volumes, average pore diameters, and proton conductivities of the sulfated ZrO_2 samples templated with $C_{16}TAB$. The sulfated ZrO_2 sample had the smallest surface area of 78 m^2/g at the $C_{16}TAB/Zr= 0.25$. Its large pore volume (0.16 cm^3/g) and mean pore size (8.2 nm) were mainly from inter-particle pores. Increased numbers of templated pores raised the surface area to 114 m^2/g and reduced the mean pore size to 2.4 nm when the $C_{16}TAB/Zr= 0.38$. Further increase in the $C_{16}TAB/Zr$ ratio to 0.50-0.63 increased the surface area to 122-128 m^2/g. The appearance of the typical pores at 3.9 nm also resulted in larger mean pore size of 2.8-3.0 nm. The sample prepared with the $C_{16}TAB/Zr$ ratio= 0.50 performed the highest proton conductivity of 20 mS/cm, whereas the $C_{16}TAB/Zr= 0.25$ led the sample exhibiting the lowest proton conductivity of 12 mS/cm. This phenomenon suggests that large surface area and small pore diameter are beneficial to the proton transportation. The texture effect is supported by the low proton conductivity of the S-ZrO_2 sample (9 mS/cm, shown in Table 4-4). The samples with the $C_{16}TAB/Zr= 0.38$ and 0.63 showed the similar proton conductivities of 16-17 mS/cm because of the compromising effects of their pore sizes and surface areas.

Table 4-3 Summaries of the BET properties and the proton conductivities of the $C_{16}S$-ZrO_2 synthesized with different CTAB/Zr molar ratios.

CTAB/Zr molar ratio	S_{BET} (m^2/g)	V_{pore} (cm^3/g)	D_{pore} (nm)	PC (mS/cm)
0.25	78	0.16	8.2	12
0.38	114	0.07	2.4	16
0.50	128	0.08	2.8	20
0.63	122	0.09	3.0	17

Addition of sulfuric acid into the precipitation system assisted the formation of the porous structure with a narrow pore size distribution. Figure 4-11 shows the N_2 adsorption/desorption isotherms and the BJH pore size distribution of the C_{16}SS-ZrO_2 sample. Mesoporous feature was found in its Type IV adsorption isotherm and H3 hysteresis loop. In contrast to the C_{16}TAB samples, the C_{16}SS-ZrO_2 powder had a narrow pore distribution which centered at 3.9 nm. Templating pathway has been demonstrated through electrostatic interaction between the templates and the hydrated oxide colloids. The Zr-OH^+-SO_4^{2-}-$C_{16}TA^+$ bonding is believed to direct the aggregation of the ZrO_2 colloids along with the self-assembly of C_{16}TAB to form their mesoporous structures. Addition of sulfuric acids improved the interaction between the template and the ZrO_2 colloids and contributed to the narrow pore size distribution. Table 4-4 lists the textural results and proton conductivities of the S-ZrO_2 (See Appendix B-1), C_{16}SS-ZrO_2, C_8S-ZrO_2 (EtOH), and C_8S-ZrO_2 (IEE) samples. The C_{16}SS-ZrO_2 powder had a surface area of 128 m^2/g, a mean pore size of 5.5 nm, and a pore volume of 0.23 cm^3/g.

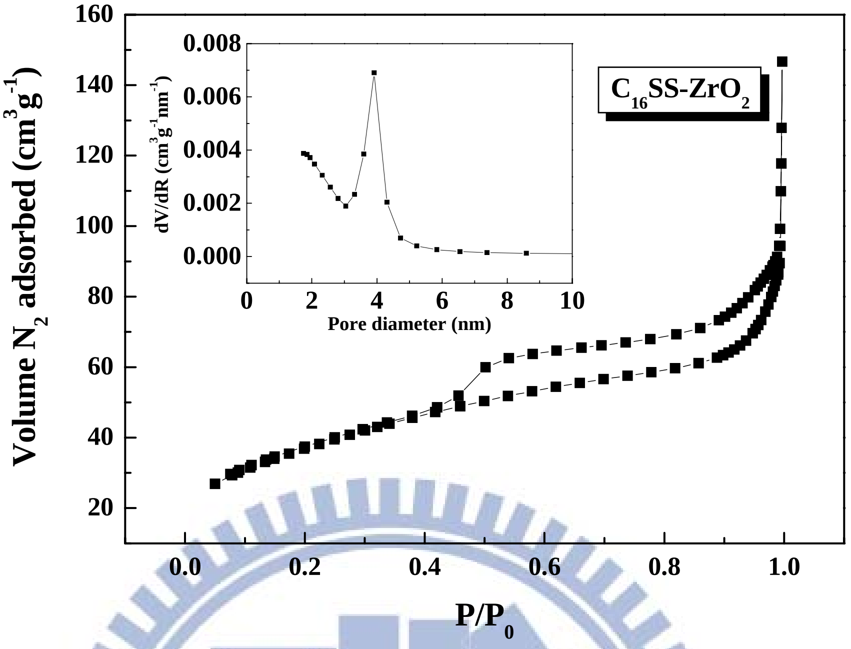

Figure 4-11 N_2 adsorption and desorption isotherm and BJH pore size distribution of the $C_{16}SS\text{-}ZrO_2$ sample.

To prepare micorporous ZrO_2 samples, the surfactant C_8TAB, was used as the template. Figure 4-12 shows the N_2 adsorption/desorption isotherms and pore size distributions of the $C_8S\text{-}ZrO_2$ samples treated with different solvent removal processes before calcination. The $C_8S\text{-}ZrO_2$ (IEE) sample exhibited Type II adsorption isotherm and a hysteresis loop ending at P/P_0= 0.8. The pore distribution ranged between 2 and 50 nm and centered at 20 nm. Ion exchange induces the pore close during the post thermal treatment, consequently leading to the small surface area of 7 m^2/g and the small pore volume of 0.04 cm^3/g. Type I adsorption[19] indicates that the micropore was preserved in the $C_8S\text{-}ZrO_2$ (EtOH) sample (Figure 4-13). The pore distribution centered at 0.5 nm, while the mean pore diameter was 0.6 nm. Small pore size resulted in the small pore volume of 0.06 cm^3/g but the high surface area of 114 m^2/g.

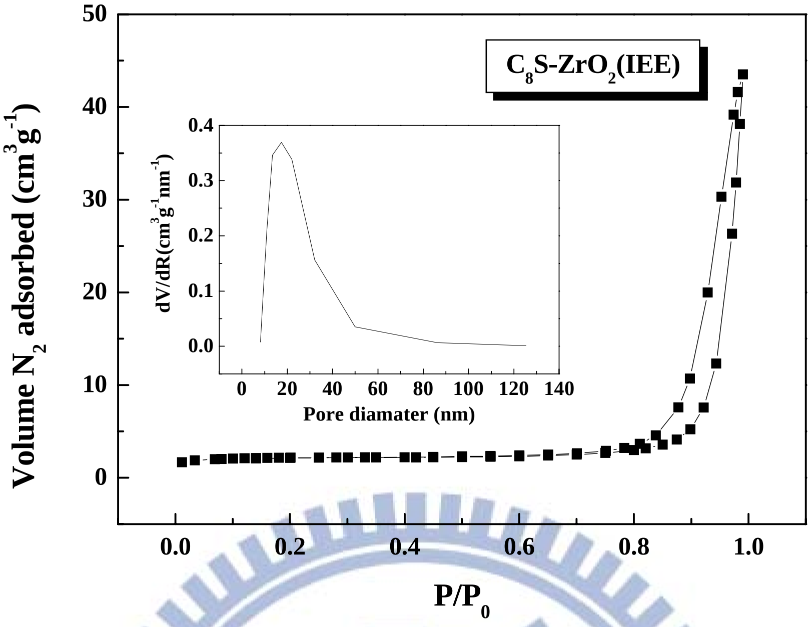

Figure 4-12 N_2 adsorption and desorption isotherm and BJH pore size distribution of C_8S-ZrO_2 (IEE)

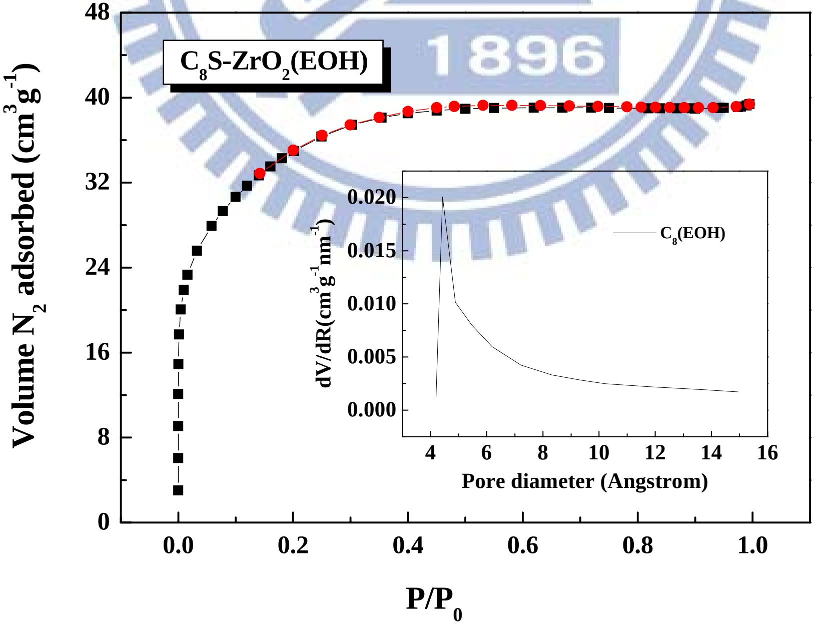

Figure 4-13 N_2 adsorption and desorption isotherm and BJH pore size distribution of C_8S-ZrO_2 (EOH) samples.

Table 4-4 The textural results and proton conductivities of S-ZrO_2, C_{16}SS-ZrO_2, C_8S-ZrO_2 (IEE) and C_8S-ZrO_2 (EtOH) samples.

Samples	S_{BET} (m^2 /g)	V $_{pore}$ (cm^3/g)	D $_{pore}$ (nm)	PC (mS/cm)
S-ZrO_2	64	0.31	16.4	9
C_{16}SS-ZrO_2	128	0.23	5.5	15
C_8S-ZrO_2 (IEE)	7	0.04	22.3	20
C_8S-ZrO_2 (EtOH)	114	0.06	0.6	26

The proton conductivities of the C_{16}SS-ZrO_2, C_8S-ZrO_2 (IEE) and C_8S-ZrO_2 (EtOH) samples were 15, 20, and 26 mS/cm, respectively. Since the C_{16}S-ZrO_2 and C_{16}SS-ZrO_2, powers had similar surface sulfated-ion loading, chemical structures, and acidity, the difference in their proton conductivity reflects the effect of pore sizes. The higher proton conductivity of the C_{16}S-ZrO_2 sample (20 mS/cm) indicates that the proton transport in the ZrO_2 matrix was improved when the mean pore size decreased from 5.5 to 2.8 nm. The C_8S-ZrO_2 (IEE) sample performed the same proton conductivity as that of the C_{16}S-ZrO_2 sample. However, this mesoporous sample exhibited the large pore size (22.3 nm) and the low surface area (7 m^2/g). This phenomenon reveals that high surface acidity is another vital parameter dominating high proton conductivity. The highest proton conductivity (26 mS/cm) was found in the microporous C_8S-ZrO_2 (EtOH) sample. The high conducting ability could be due to its small pore size (0.6 nm) or high surface loading of pyrosulfate species (S/Zr= 0.38). To understand the effect of surface sulfate density on the proton transport efficiency, we further examine the proton conductivity of the C_{16}S-ZrO_2 sample post-treated with sulfuric acid at different concentrations.

4-6. Post sulfation

The surface compositions and chemical states of the sulfated ZrO_2 samples post treated with sulfuric acid were characterized using XPS (see Appendix A-2). Table 4-5 lists the surface and total S/Zr ratios of the $C_{16}S$-ZrO_2 samples impreganated with sulfuric acid at different concentrations. The surface S/Zr ratio increased from 0.19 to 0.27 when the concentration of sulfuric acid increased from 0.3 to 1.2 M. However, the total S/Zr ratio was maintained at $2.0\text{-}2.1\times 10^{-2}$ over the different concentrations, except for 0.9 M which remarkably increased the ratio to 18.5×10^{-2}. The O-S/S, O-Zr/Zr, and O-H/Zr ratios of these post sulfation samples are summarized in Table 4-6. The O-S/S ratios were in the range of 3.41-3.53, indicating pyrosulfate ($S_2O_7^{2-}$) species. Post sulfation slightly decreased the O-Z/Zr ratio from 1.89 to 2.28, but greatly decreasing the O-H/Zr ratio from 0.20 to 0.12 at 0.9-1.2 M. These findings reveal that the sulfate ions diffuse into the mesopores and are adsorbed on the ZrO_2 surface, where are free from the bonded sulfate species, at low concentrations (< 0.9 M). Over concentrated sulfate acid exhibited high surface tension, thus inhibiting their diffusion into the mesoporous channels. Calcination drove the adsorbed sulfate ions forming pyrosulfate species through dehydration.

Table 4-5 The total and surface S/Zr ratios of the $C_{16}S\text{-}ZrO_2$ sample post treated with sulfuric acid at different concentrations.

	S-to-Zr atomic ratio	
Samples	Total	Surface
$C_{16}S\text{-}ZrO_2$-0.3 M	2.0×10^{-2}	0.19
$C_{16}S\text{-}ZrO_2$-0.6 M	2.1×10^{-2}	0.20
$C_{16}S\text{-}ZrO_2$-0.9 M	18.5×10^{-2}	0.25
$C_{16}S\text{-}ZrO_2$-1.2 M	2.1×10^{-2}	0.27

Table 4-6 The O-S/S, O-Zr/Zr, and O-H/Zr ratios of the C16S-ZrO2 sample impregnated with sulfuric acid at different concentrations.

Samples	O-S/S	(O-Zr)/Zr	O-H/Zr
$C_{16}S\text{-}ZrO_2$-0.3 M	3.53	1.89	0.23
$C_{16}S\text{-}ZrO_2$-0.6 M	3.45	2.28	0.29
$C_{16}S\text{-}ZrO_2$-0.9 M	3.43	1.93	0.12
$C_{16}S\text{-}ZrO_2$-1.2 M	3.41	1.95	0.12

Figure 4-14 shows the NH_3-TPD curves of the post sulfation samples. Increase in the desorption intensity at 290 °C was found after impregnation of the sulfated ZrO_2 powders with sulfuric acid. This result indicates that high density of pyrosulfate species raises the surface acidity.

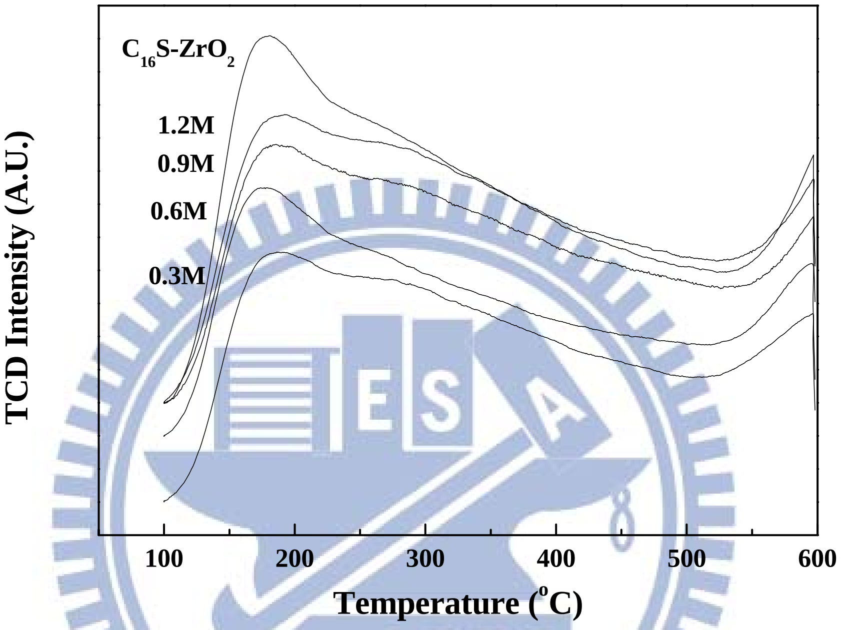

Figure 4-14 NH_3 TPD patterns for $C_{16}S$-ZrO_2 (CTAB/Zr= 0.5) and which impregnated with different concentrations of H_2SO_4.

Type IV adsorptions and characteristic hysteresis loops were sill observed in the post sulfation samples. (see Appendix B-2) Similar pore distribution was also found when the pore size was smaller than 3.0 nm. However, two typical pore sizes at 3.5 and 4.1 nm were resulted after the post treatment. Relative to the single peak at 3.9 nm in the $C_{16}S$-ZrO_2 powders, the larger pores resulted from the thermal induced pore collapse, while the deposition of sulfate ions on the inner pore wall surface reduced the pore sizes.

Table 4-7 summarizes the textural data of post sulfated $C_{16}S$-ZrO_2 samples and their corresponding proton conductivities. Post sulfation slightly reduced the specific surface area from 128 to 113 m^2/g. Loading sulfate ions in the pore channels decreased the mean pore size from 3.0 to 2.8 nm when the concentration of sulfuric acid decreased from 0.3 to 0.9 M. Larger mean pore size of 3.1 nm was obtained at 1.2 M because of inefficient diffusion of the sulfate ions into the mesopores. This result was in agreement with its low total S/Zr ratio but high surface sulfur density. Post sulfation effectively increased the proton conductivity of the mesoporous sulfated ZrO_2 sample. The conductivity was remarkably improved by 1.5, 3.5, and 4.8 fold to be 31, 69, and 95 mS/cm, respectively, at 0.3, 0.6, and 0.9 M. The pronton conductivity of the $C_{16}S$-ZrO_2-0.6M and $C_{16}S$-ZrO_2-0.6M samples even were 1.3 and 1.8 times higher than that of Nafion (52 mS/cm). These results clearly evidence the highly potential of the inorganic solid acids to be the alternatives for the electrolyte. Moreover, the high loading of pyrosulfate species and strong surface acidity are responsible for the high proton conducting ability. The proton conductivity decreased to 42 mS/cm at 1.2 M because of fewer amounts of pyrosulfate in the inner pore wall. Compared to the post sulfation samples, the C_8S-ZrO_2 (EtOH) sample had the highest surface S/Zr ratio of 0.38. Its low proton conductivity (26 mS/cm) reveals that the micropores (mean pore size of 0.6 nm) limit proton transport. Therefore, the optimal pore size for the high proton conductivity is in the range of 0.6-2.8 nm.

Table 4-7 The textural properties and the proton conductivities of the $C_{16}S$-ZrO_2 powders after post sulfation.

Concentration of H_2SO_4	S_{BET} (m^2 /g)	V $_{pore}$ (cm^3/g)	D $_{pore}$ (nm)	PC (mS/cm)
$C_{16}S$-ZrO_2-0.3 M	121	0.09	3.0	31
$C_{16}S$-ZrO_2-0.6 M	128	0.10	2.9	69
$C_{16}S$-ZrO_2-0.9 M	119	0.09	2.8	95
$C_{16}S$-ZrO_2-1.2 M	113	0.09	3.1	42

4-7 Water content

Water plays an important role in conveying proton through the solid electrolytes, and it has been demonstrated that the water content and the interaction between the water molecules and surface acid sites control the proton conductivity of the solid electrolytes. Numerous researchers designed their materials as porous structures or functionalized the porous materials with some acid groups to increase the water content at high temperature. In this study, we measure the weight loss of the sulfated ZrO_2 samples at elevated temperatures to understand their ability for maintaining water molecules and the dependence of the proton conductivity upon their textures and surface acidity. Table 4-8 lists the water content, proton conductivity and pore diameter of all sulfated ZrO_2 samples. The total water content (WC_{total}) in the samples was determined by the weight loss from room temperature (RT) to 400°C. The weight losses from 100°C to 400°C ($WC_{100-400}$) represent the water attracted in the small meso- or micro-pore channels. We used the $WC_{100-400}$/ WC_{total} ratio to indicate the capability of the samples for keeping water molecules at high temperatures. The S-ZrO_2 had the lowest $WC_{100-400}$/ WC_{total} ratio of 4.1 and the largest pore size of 16.4 nm, moreover the lowest proton conductivity of 9 mS cm^{-1}. It means that this size of pore had the weakest adsorption energy for water and the weakest proton transportation ability. Templating method allows the C_{16}S-ZrO_2 and the C_{16}SS-ZrO_2 sample exhibiting small pore size of 2.8-5.5 nm. Correspondingly, the higher $WC_{100-400}$/ WC_{total} ratios ranged between 12-18.6 were obtained. The proton conductivity of these two samples (C_{16}S-ZrO_2 and C_{16}SS-ZrO_2) is almost two times higher than S-ZrO_2 samples. A similar phenomenon was reported by Sayler et al.[73]. The correlation between electrical conductivity, relative humidity, and pore connectivity in Mesoporous Silica Monoliths was discussed. They found that Monoliths (20-30 nm) without surfactant templated mesopores exhibit no electrical conductivity until the humidity is high enough for the textural mesopores to begin to fill. For C_{18}TAB templated silica (4-5 nm), the mesopores form extensive networks, which fill at low relative humidity to provide a continuous path for electrical conductivity over macroscopic distances. It is found that the $C_8S\text{-}ZrO_2$ (EtOH) sample had the smallest pore diameter of 0.6 nm and showed the largest $WC_{100\text{-}400}/WC_{total}$ ratio of 23. The intermolecular interaction between the surface acid molecules and the water increase as the pore size gets smaller. A similar phenomenon was reported by Hara [19] and Ghosh [34]. In their study, water molecules were tightly adsorbed in microprous structures because of high adsorption energy. In contrast to the $C_{16}S\text{-}ZrO_2$ and the $C_{16}SS\text{-}ZrO_2$ sample, the $C_8S\text{-}ZrO_2$ (EtOH) sample showed the lower proton conductivity of 20 mS/cm. Since the size of water molecular is about 3 Å, and it is only 2 water molecules available to be filled in the micropore channels of the $C_8S\text{-}ZrO_2$ (EtOH) sample. According to the Grotthuss mechanisms, the proton exists as hydronium ion ($H_5O_2^+$ or $H_9O_4^+$) and migrates in the central of channels. In this study, the water molecules are too tightly bound on the surface acid sites to diffuse across the microporous channels. The highest $WC_{100\text{-}400}/WC_{total}$ ratio (26.4) also was found in $C_8S\text{-}ZrO_2$ (IEE) sample which showed the largest pore size of 22.3 nm. The strong water adsorption is due to its high surface acidity. However, its proton conductivity (20 mS/cm) was lower than the $C_8S\text{-}ZrO_2$ (EtOH) sample (26 mS/cm). This phenomenon is in agreement with the low proton conductivity of the $S\text{-}ZrO_2$ sample. Therefore, it exists optimal pore-size ranging from 0.6 to 2.8 nm for high proton conductivity.

Post sulfation greatly decreased the $WC_{100\text{-}400}/WC_{total}$ ratio of the $C_{16}S\text{-}ZrO_2$ sample from 18.6 to 9.8-12.9 even though it increased the surface acidity. In contrast to the $C_{16}S\text{-}ZrO_2$ sample, the conductivity of the post sulfated sample was remarkably increased from 20 to 31-95 mS/cm. These results reveal that appropriate surface acidity which exhibit adequate adsorption energy for water is required for efficient proton transport. Datta et al. [48] found that the hindrance of proton transfer is most likely due to the attraction of proton by the negatively charged sulfonate groups of Nafion when it is dried. In the presence of less amount of water, the shielding of the oppositely charged ions from each other is significantly reduced, so that retarding the movement of the proton. In summary, both the pore sizes and surface acidity determine the adsorption capability for water molecules. An optimal combination of these two features can contribute to high proton conductivity.

Table 4-8 The water content, proton conductivity and pore size of all sulfated ZrO_2 samples.

Sample	**WC_{total} (RT-400°C)**	**$WC_{100-400}$ (100-400°C)**	**$WC_{100-400}/WC_{total}$ ($\times 10^{-2}$)**	**Proton Conductivity (mS/cm)**	**Pore diameter (nm)**
S-ZrO_2	31.5% [a]	1.3%	4.1	9	16.4
C_{16}S-ZrO_2	27.4%	5.1%	18.6	20	2.8
C_{16}SS-ZrO_2	25.8%	3.1%	12.0	15	5.5
C_{16}S-ZrO_2-0.3M	26.7%	2.7%	10.1	31	3.0
C_{16}S-ZrO_2-0.6M	21.7%	2.8%	12.9	69	2.9
C_{16}S-ZrO_2-0.9M	23.6%	3.0%	12.7	95	2.8
C_{16}S-ZrO_2-1.2M	29.6%	2.9%	9.8	42	3.1
C_8S-ZrO_2(IEE)	50.4%	13.3%	26.4	20	22.3
C_8S-ZrO_2(EtOH)	17.2%	4.1%	23.8	26	0.6

a- weight loss %

Chapter 5. Summary

5-1. Conclusions

The dependence of proton conductivities upon the pore sizes and surface properties of sulfated ZrO_2 powders are compared and discussed. The proton conductivity increases with increasing surface areas. In contrast, it increases as pore sizes decrease. Reduction in the pore size enhances the conductivity till 2.8 nm. Post sulfation of the mesoporous ZrO_2 samples with a 0.9 M H_2SO_4 solution increases their bulk content of sulfated species by 9 times and effectively promotes the conductivity from 2.0 to 9.5×10^{-2} S/cm. This value is twice higher than that of the commercial Nafion (5.2×10^{-2} S/cm). Polysulfated species, which is produced after calcination of the S-doped ZrO_2 samples, introduces strong surface acid sites and contributes to the high proton conductivity. Both high surface acidity and microporous structure improve the capability of the samples for keeping water molecules at high temperatures. However, the highest proton conductivity was not given by these samples with the highest surface acidity or microporous texture. Appropriate surface acidity and pore size which exhibit adequate adsorption energy for water is required for efficient proton transport. In summary, an optimal combination of both the pore size (0.6-2.8 nm) and surface acidity can contribute to high proton conductivity.

References

1. H.L. Lin, T.L. Yu, and F.H. Han, "A Method for Improving Ionic Conductivity of Nafion Membranes and its Application to PEMFC". *Journal of Polymer Research*, **2006**, 13(5), 379-385.
2. S. Paddison, "Proton conduction mechanisms at low degrees of hydration in sulfonic acid-based polymer electrolyte membranes". *Annual Review of Materials Research*, **2003**, 33(1), 289-319.
3. P. Choi, N.H. Jalani, and R. Datta, "Thermodynamics and proton transport in Nafion". *Journal of The Electrochemical Society*, **2005**, 152E123.
4. S. Slade, S. Campbell, T. Ralph, and F. Walsh, "Ionic conductivity of an extruded Nafion 1100 EW series of membranes". *Journal of The Electrochemical Society*, **2002**, 149A1556.
5. E. Spohr, "Proton transport in polymer electrolyte fuel cell membranes". *Ionic soft matter: modern trends in theory and applications*, **2005**, 361-379.
6. R. Marschall, J. Rathousky, and M. Wark, "Ordered Functionalized Silica Materials with High Proton Conductivity". *Chemistry of Materials*, **2007**, 19(26), 6401-6407.
7. P. CHOI, N.H. JALANI, and R. DATTA, "Thermodynamics and proton transport in Nafion. II. Proton diffusion mechanisms and conductivity". *Journal of The Electrochemical Society*, **2005**, 152(3), E123-E130.
8. M. Navarra, F. Croce, and B. Scrosati, "New, high temperature superacid zirconia-doped Nafion(tm) composite membranes". *J. Mater. Chem.*, **2007**, 17(30), 3210-3215.
9. A. D¡¦Epifanio, M.A. Navarra, F.C. Weise, B. Mecheri, J. Farrington, S. Licoccia, and S. Greenbaum, "Composite Nafion/Sulfated Zirconia Membranes: Effect of the Filler Surface Properties on Proton Transport Characteristics". *Chemistry of Materials*, **2009**, 22(3), 813-821.
10. S. Zaidi, S.D. Mikhailenko, G. Robertson, M. Guiver, and S. Kaliaguine, "Proton conducting composite membranes from polyether ether ketone and heteropolyacids for fuel cell applications". *Journal of Membrane Science*, **2000**, 173(1), 17-34.
11. M. Nogami, R. Nagao, C. Wong, T. Kasuga, and T. Hayakawa, "High Proton Conductivity in porous P2O5-SiO2 Glasses". *The Journal of Physical Chemistry B*, **1999**, 103(44), 9468-9472.
12. F.M. Vichi, M.I. Tejedor-Tejedor, and M.A. Anderson, "Effect of pore-wall chemistry on proton conductivity in mesoporous titanium dioxide". *Chemistry of Materials*, **2000**, 12(6), 1762-1770.

13. C.Y. Tai, B.Y. Hsiao, and H.Y. Chiu, "Preparation of spherical hydrous-zirconia nanoparticles by low temperature hydrolysis in a reverse microemulsion". *Colloids and Surfaces A: Physicochemical and Engineering Aspects*, **2004**, 237(1-3), 105-111.
14. D.R. Rolison, P.L. Hagans, K.E. Swider, and J.W. Long, "Role of hydrous ruthenium oxide in Pt-Ru direct methanol fuel cell anode electrocatalysts: the importance of mixed electron/proton conductivity". *Langmuir*, **1999**, 15(3), 774-779.
15. S. Hara and M. Miyayama, "Proton conductivity of superacidic sulfated zirconia". *Solid State Ionics*, **2004**, 168(1-2), 111-116.
16. C. Morterra, G. Cerrato, F. Pinna, and M. Signoretto, "Brosted Acidity of a Superacid Sulfate-Doped ZrO2 System". *The Journal of Physical Chemistry*, **1994**, 98(47), 12373-12381.
17. C. Kresge, M. Leonowicz, W. Roth, J. Vartuli, and J. Beck, "Ordered mesoporous molecular sieves synthesized by a liquid-crystal template mechanism". *Nature*, **1992**, 359(6397), 710-712.
18. H. Zhou, D. Li, M. Hibino, and I. Honma, "A Self Ordered, Crystalline¡VGlass, Mesoporous Nanocomposite for Use as a Lithium Based Storage Device with Both High Power and High Energy Densities". *Angewandte Chemie International Edition*, **2005**, 44(5), 797-802.
19. S. Hara, S. Takano, and M. Miyayama, "Proton-conducting properties and microstructure of hydrated tin dioxide and hydrated zirconia". *The Journal of Physical Chemistry B*, **2004**, 108(18), 5634-5639.
20. S. Srinivasan, *Fuel cells: from fundamentals to applications*2006: Springer Verlag.
21. T. Gierke, G. Munn, and F. Wilson, "The morphology in nafion perfluorinated membrane products, as determined by wide and small angle x ray studies". *Journal of Polymer Science: Polymer Physics Edition*, **1981**, 19(11), 1687-1704.
22. T. Gierke, "GE MUNN and FC WILSON". *Journal of Polymer Science Part B-Polymer Physics*, **1981**, 19(11),
23. K. Schmidt-Rohr and Q. Chen, "Parallel cylindrical water nanochannels in Nafion fuel-cell membranes". *Nature materials*, **2007**, 7(1), 75-83.
24. K.D. Kreuer, S.J. Paddison, E. Spohr, and M. Schuster, "Transport in proton conductors for fuel-cell applications: Simulations, elementary reactions, and phenomenology". *Chemical Reviews*, **2004**, 104(10), 4637-4678.
25. C.H. Lee, H.B. Park, Y.M. Lee, and R.D. Lee, "Importance of proton conductivity measurement in polymer electrolyte membrane for fuel cell application". *Industrial & engineering chemistry research*, **2005**, 44(20), 7617-7626.
26. Y. Sone, P. Ekdunge, and D. Simonsson, "Proton Conductivity of Nafion 117 as Measured by a Four Electrode AC Impedance Method". *Journal of The Electrochemical Society*, **1996**, 1431254.

27. X. Yuan, H. Wang, J. Colin Sun, and J. Zhang, "AC impedance technique in PEM fuel cell diagnosis--A review". *International Journal of Hydrogen Energy*, **2007**, 32(17), 4365-4380.

28. B.A. Holmberg and Y. Yan, "An apparatus for direct proton conductivity measurement of powdered materials". *Journal of The Electrochemical Society*, **2006**, 153A146.

29. C. Ho, I. Raistrick, and R. Huggins, "Application of A C Techniques to the Study of Lithium Diffusion in Tungsten Trioxide Thin Films". *Journal of The Electrochemical Society*, **1980**, 127343.

30. M.A. Barique, L. Wu, N. Takimoto, K. Kidena, and A. Ohira, "Effect of Water on the Changes in Morphology and Proton Conductivity for the Highly Crystalline Hydrocarbon Polymer Electrolyte Membrane for Fuel Cells". *The Journal of Physical Chemistry B*, **2009**, 113(49), 15921-15927.

31. W. Zhang, P.L. Yue, and P. Gao, "Crystallinity Enhancement of Nafion Electrolyte Membranes Assisted by a Molecular Gelator". *Langmuir*, **2011**,

32. K. Matsumoto, T. Higashihara, and M. Ueda, "Locally and densely sulfonated poly (ether sulfone) s as proton exchange membrane". *Macromolecules*, **2009**, 42(4), 1161-1166.

33. K. Xu, H. Oh, M.A. Hickner, and Q. Wang, "Highly Conductive Aromatic Ionomers with Perfluorosulfonic Acid Side Chains for Elevated Temperature Fuel Cells". *Macromolecules*, **2011**,

34. Y. Yao, L. Ji, Z. Lin, Y. Li, M. Alcoutlabi, H. Hamouda, and X. Zhang, "Sulfonated Polystyrene Fiber Network-Induced Hybrid Proton Exchange Membranes". *ACS Applied Materials & Interfaces*, **2011**,

35. B.D. Ghosh, K.F. Lott, and J.E. Ritchie, "Conductivity dependence of PEG content in an anhydrous proton conducting sol-gel electrolyte". *Chemistry of Materials*, **2005**, 17(3), 661-669.

36. D. Truffier-Boutry, A. De Geyer, L. Guetaz, O. Diat, and G. Gebel, "Structural study of zirconium phosphate-Nafion hybrid membranes for high-temperature proton exchange membrane fuel cell applications". *Macromolecules*, **2007**, 40(23), 8259-8264.

37. H. Zarrin, D. Higgins, J. Yu, M. Fowler, and Z. Chen, "Functionalized Graphene Oxide Nanocomposite Membrane for Low Humidity and High Temperature Proton Exchange Membrane Fuel Cells". *The Journal of Physical Chemistry C*, **2011**,

38. B.P. Tripathi and V.K. Shahi, "Functionalized Organic− Inorganic Nanostructured N-p-Carboxy Benzyl Chitosan− Silica− PVA Hybrid Polyelectrolyte Complex as Proton Exchange Membrane for DMFC Applications". *The Journal of Physical Chemistry B*, **2008**, 112(49), 15678-15690.

39. M.K. Mistry, N.R. Choudhury, N.K. Dutta, R. Knott, Z. Shi, and S. Holdcroft, "Novel

Organic− Inorganic Hybrids with Increased Water Retention for Elevated Temperature Proton Exchange Membrane Application". *Chemistry of Materials*, **2008**, 20(21), 6857-6870.

40. R. Marschall, J. Rathouský, and M. Wark, "Ordered Functionalized Silica Materials with High Proton Conductivity". *Chemistry of Materials*, **2007**, 19(26), 6401-6407.
41. J.C. McKeen, Y.S. Yan, and M.E. Davis, "Proton conductivity in sulfonic acid-functionalized zeolite beta: effect of hydroxyl group". *Chemistry of Materials*, **2008**, 20(12), 3791-3793.
42. S. Tominaka, N. Akiyama, F. Croce, T. Momma, B. Scrosati, and T. Osaka, "Sulfated zirconia nanoparticles as a proton conductor for fuel cell electrodes". *Journal of Power Sources*, **2008**, 185(2), 656-663.
43. G.L. Athens, D. Kim, J.D. Epping, S. Cadars, Y. Ein-Eli, and B.F. Chmelka, "Molecular Optimization of Multiply-Functionalized Mesoporous Films with Ion Conduction Properties". *Journal of the American Chemical Society*, **2011**,
44. J. Zeng and S.P. Jiang, "Characterization of High-Temperature Proton-Exchange Membranes Based on Phosphotungstic Acid Functionalized Mesoporous Silica Nanocomposites for Fuel Cells". *The Journal of Physical Chemistry C*, **2011**,
45. T.J. Peckham, J. Schmeisser, and S. Holdcroft, "Relationships of acid and water content to proton transport in statistically sulfonated proton exchange membranes: variation of water content via control of relative humidity". *The Journal of Physical Chemistry B*, **2008**, 112(10), 2848-2858.
46. M. Saito, K. Hayamizu, and T. Okada, "Temperature dependence of ion and water transport in perfluorinated ionomer membranes for fuel cells". *The Journal of Physical Chemistry B*, **2005**, 109(8), 3112-3119.
47. D.E. Moilanen, D. Spry, and M. Fayer, "Water dynamics and proton transfer in Nafion fuel cell membranes". *Langmuir*, **2008**, 24(8), 3690-3698.
48. K. Kunimatsu, B. Bae, K. Miyatake, H. Uchida, and M. Watanabe, "ATR-FTIR Study of Water in Nafion Membrane Combined with Proton Conductivity Measurements during Hydration/Dehydration Cycle". *The Journal of Physical Chemistry B*, **2011**,
49. E.S.S. Iyer and A. Datta, "Importance of Electrostatic Interactions in The Mobility of Cations in Nafion". *Journal of Physical Chemistry B*, **2011**, 115(27), 8707-8712.
50. B.M. Reddy and M.K. Patil, "Organic syntheses and transformations catalyzed by sulfated zirconia". *Chemical Reviews*, **2009**, 109(6), 2185-2208.
51. N.H. Jalani, K. Dunn, and R. Datta, "Synthesis and characterization of Nafion -MO2 (M= Zr, Si, Ti) nanocomposite membranes for higher temperature PEM fuel cells". *Electrochimica acta*, **2005**, 51(3), 553-560.
52. M. Yamada, D. Li, I. Honma, and H. Zhou, "A Self-Ordered, Crystalline Glass, Mesoporous Nanocomposite with High Proton Conductivity of 2× 10-2 S cm-1 at

Intermediate Temperature". *Journal of the American Chemical Society*, **2005**, 127(38), 13092-13093.

53. B. Yameen, A. Kaltbeitzel, A. Langner, H. Duran, F. Mueller, U. Goesele, O. Azzaroni, and W. Knoll, "Facile large-scale fabrication of proton conducting channels". *Journal of the American Chemical Society*, **2008**, 130(39), 13140-13144.
54. Manish. K. Mishra, B. Tyagi, and R.V. Jasra*, "Effect of synthetic parameters on structural, textural, and catalytic properties of nanocrystalline sulfated zirconia prepared by sol-gel technique". *Industrial & engineering chemistry research*, **2003**, 42(23), 5727-5736.
55. T. Jin, T. Yamaguchi, and K. Tanabe, "Mechanism of acidity generation on sulfur-promoted metal oxides". *The Journal of Physical Chemistry*, **1986**, 90(20), 4794-4796.
56. L. Kustov, V. Kazansky, F. Figueras, and D. Tichit, "Investigation of the Acidic Properties of ZrO2 Modified by SO2-4 Anions". *Journal of Catalysis*, **1994**, 150(1), 143-149.
57. S.Y. Chen, L.Y. Jang, and S. Cheng, "Synthesis of thermally stable zirconia-based mesoporous materials via a facile post-treatment". *The Journal of Physical Chemistry B*, **2006**, 110(24), 11761-11771.
58. U. Ciesla, M. Froba, G. Stucky, and F. Schuth, "Highly ordered porous zirconias from surfactant-controlled syntheses: Zirconium oxide-sulfate and zirconium oxo phosphate". *Chemistry of Materials*, **1999**, 11(2), 227-234.
59. C.S. Griffith, G.D. Sizgek, E. Sizgek, N. Scales, P.J. Yee, and V. Luca, "Mesoporous Zirconium Titanium Oxides. Part 1: Porosity Modulation and Adsorption Properties of Xerogels". *Langmuir*, **2008**, 24(21), 12312-12322.
60. J.Y. Ying, C.P. Mehnert, and M.S. Wong, "Synthesis and Applications of Supramolecular Templated Mesoporous Materials". *Angewandte Chemie International Edition*, **1999**, 38(1 2), 56-77.
61. G.D. Stucky, A. Monnier, F. Schuth, Q. Huo, D. Margolese, D. Kumar, M. Krishnamurty, P. Petroff, A. Firouzi, M. Janicke, and B.F. Chmelka, "MOLECULAR AND ATOMIC ARRAYS IN NANOPOROUS AND MESOPOROUS MATERIALS SYNTHESIS". *Molecular Crystals and Liquid Crystals Science and Technology Section a-Molecular Crystals and Liquid Crystals*, **1994**, 240187-200.
62. U. Ciesla and F. Schuth, "Ordered mesoporous materials". *Microporous and Mesoporous Materials*, **1999**, 27(2-3), 131-149.
63. F. Ne, F. Testard, T. Zemb, and I. Grillo, "How does ZrO2/surfactant mesophase nucleate? Formation mechanism". *Langmuir*, **2003**, 19(20), 8503-8510.
64. A. Hofmann and J. Sauer, "Surface structure of hydroxylated and sulfated zirconia. A periodic density-functional study". *The Journal of Physical Chemistry B*, **2004**,

108(38), 14652-14662.

65. R. Marcus, U. Diebold, and R.D. Gonzalez, "The locus of sulfate sites on sulfated zirconia". *Catalysis letters*, **2003**, 86(4), 151-156.

66. D.R. Milburn, R.A. Keogh, D.E. Sparks, and B.H. Davis, "XPS investigation of an iron/manganese/sulfated zirconia catalyst". *Applied surface science*, **1998**, 126(1-2), 11-15.

67. C.L. Bianchi, S. Ardizzone, and G. Cappelletti, "Surface state of sulfated zirconia: the role of the sol¡Vgel reaction parameters". *Surface and interface analysis*, **2004**, 36(8), 745-748.

68. M. Hino, M. Kurashige, H. Matsuhashi, and K. Arata, "The surface structure of sulfated zirconia: Studies of XPS and thermal analysis". *Thermochimica acta*, **2006**, 441(1), 35-41.

69. N. Lang and A. Tuel, "A fast and efficient ion-exchange procedure to remove surfactant molecules from MCM-41 materials". *Chemistry of Materials*, **2004**, 16(10), 1961-1966.

70. N. Tangchupong, W. Khaodee, B. Jongsomjit, N. Laosiripojana, P. Praserthdam, and S. Assabumrungrat, "Effect of calcination temperature on characteristics of sulfated zirconia and its application as catalyst for isosynthesis". *Fuel Processing Technology*, **2010**, 91(1), 121-126.

71. H. Shibata, T. Morita, T. Ogura, K. Nishio, H. Sakai, M. Abe, and M. Matsumoto, "Preparation and mesostructure control of highly ordered zirconia particles having crystalline walls". *Journal of materials science*, **2009**, 44(10), 2541-2547.

72. Q. Yuan, L.L. Li, S.L. Lu, H.H. Duan, Z.X. Li, Y.X. Zhu, and C.H. Yan, "Facile synthesis of Zr-based functional materials with highly ordered mesoporous structures". *The Journal of Physical Chemistry C*, **2009**, 113(10), 4117-4124.

73. F. Maddox Sayler, M.G. Bakker, J.H. Smått, and M. Lindén, "Correlation between Electrical Conductivity, Relative Humidity, and Pore Connectivity in Mesoporous Silica Monoliths". *The Journal of Physical Chemistry C*, **2010**, 114(19), 8710-8716.

Appendix A. XPS patterns of S-ZrO_2

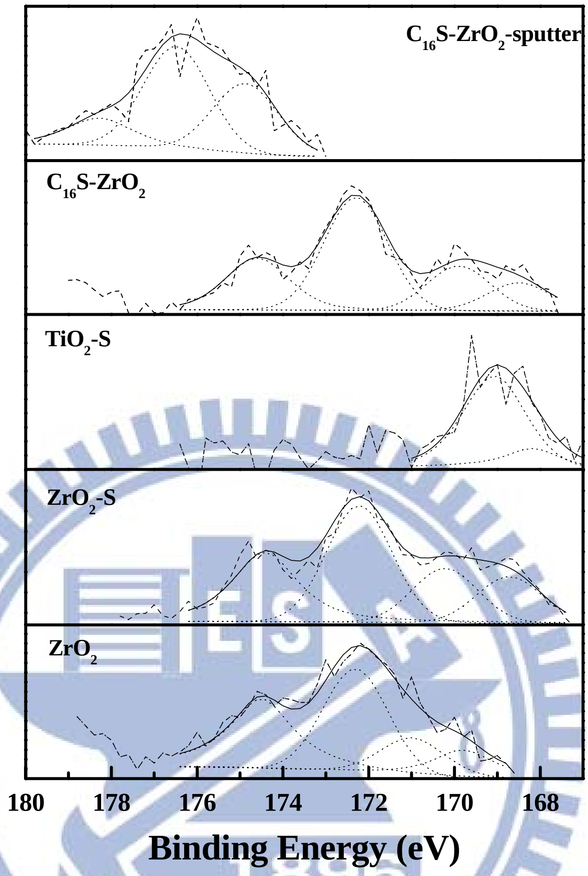

Appendix A-1 XPS patterns of pure ZrO_2

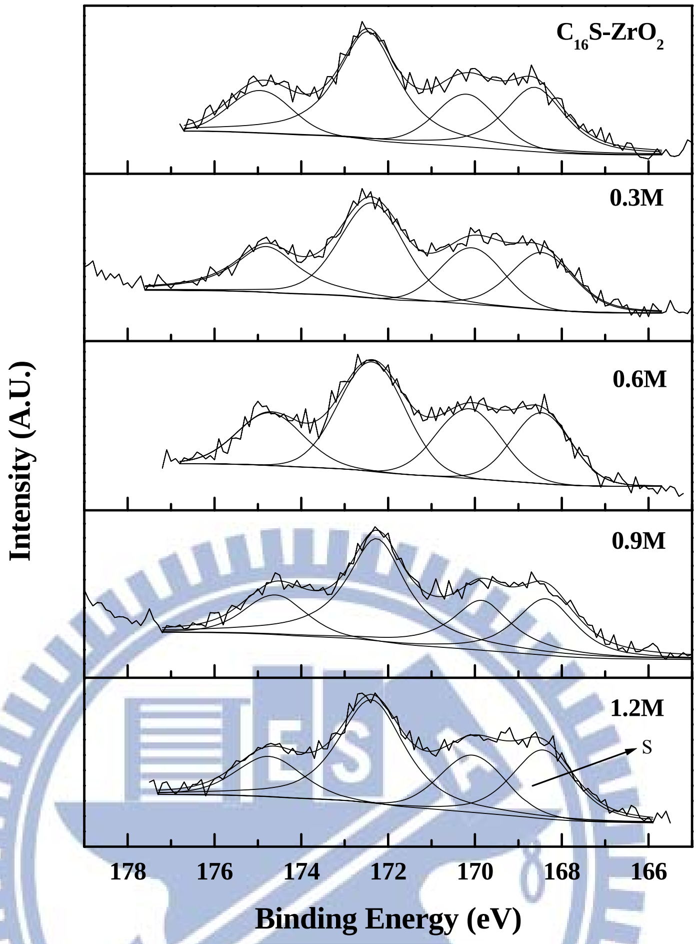

Appendix A-2 The S (2p) XPS spectra of the $C_{16}S-ZrO_2$ impregnated with sulfuric acid at different concentrations.

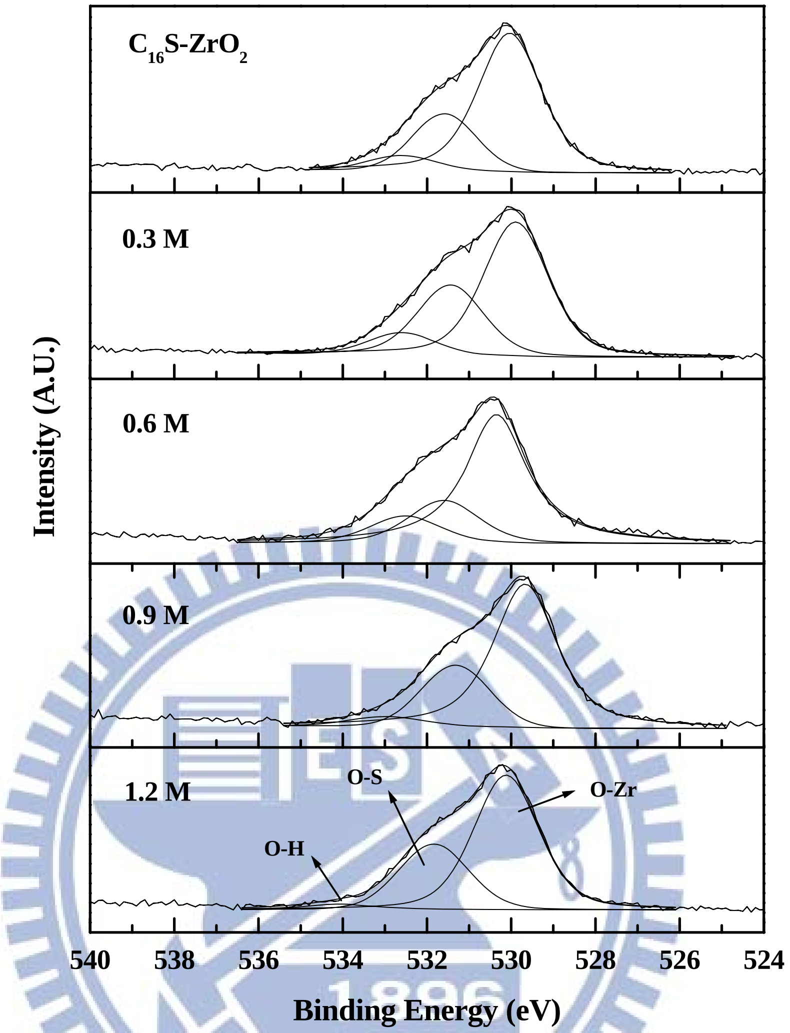

Appendix A-3 The O (1s) XPS spectra of the $C_{16}S$-ZrO_2 impregnated with sulfuric acid at different concentrations.

Appendix B. N_2 adsorption and desorption isotherm and BJH pore size distribution of S-ZrO_2.

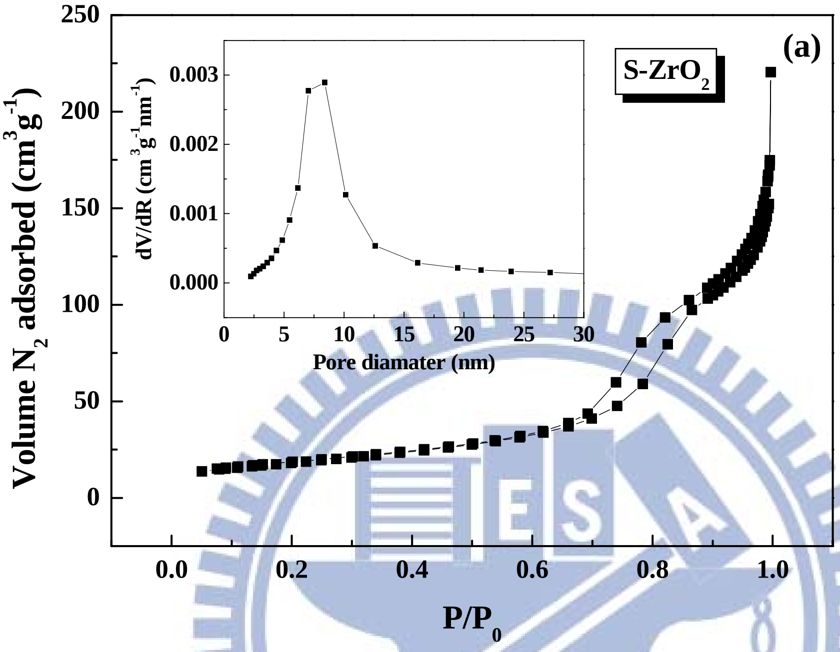

Appendix B-1 N_2 adsorption and desorption isotherm and BJH pore size distribution of S-ZrO_2.

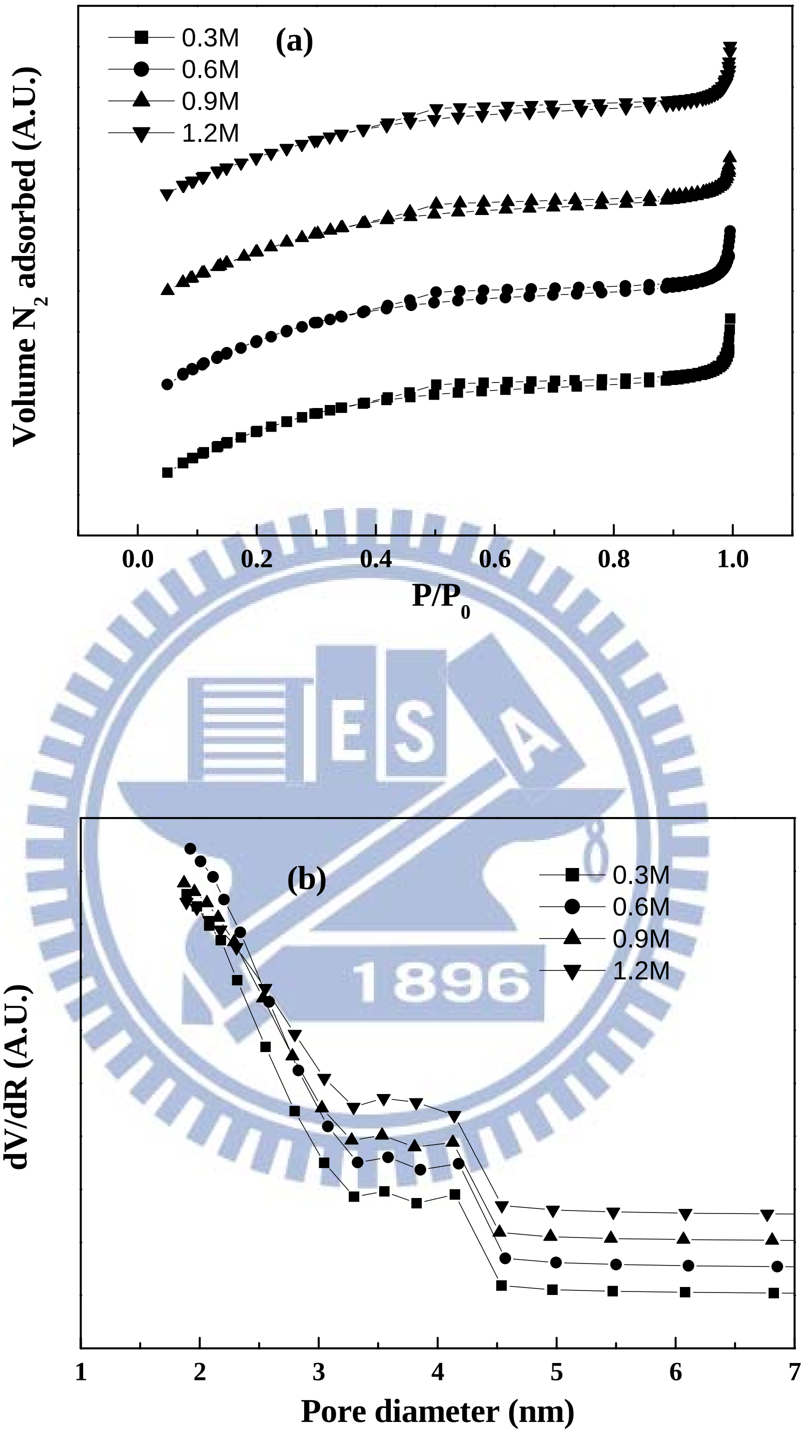

Appendix B-2 (a) Nitrogen adsorption-desorption isotherms and (b) the corresponding pore size distributions of the $C_{16}S$-ZrO_2 sample impregnated with sulfuric acid at different concentrations.

Appendix C. SEM images of sulfatd ZrO_2

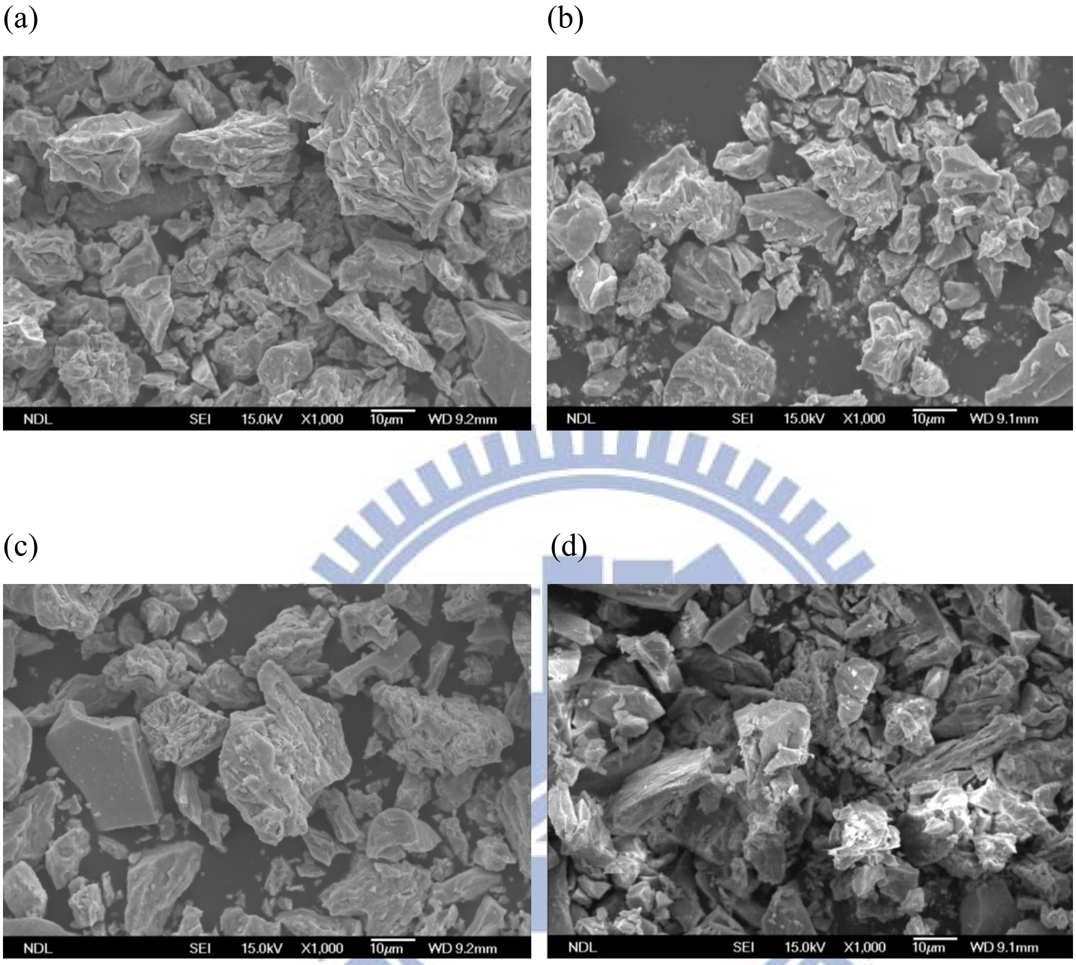

Appendix C-1 SEM images for the $C_{16}S$-ZrO_2 synthesized with different CTAB/Zr molar ratios. (a) 0.25 (b) 0.38 (c) 0.50 (d) 0.63

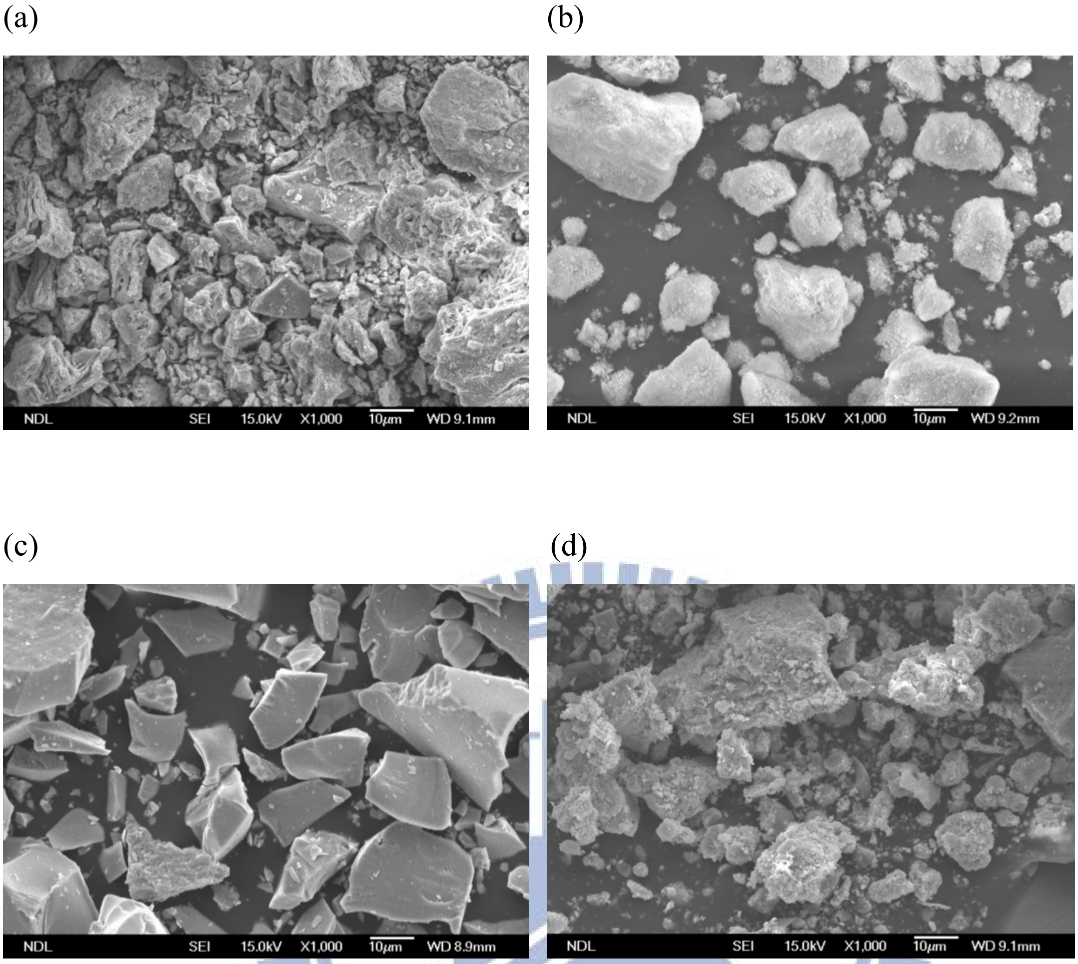

Appendix C-2 SEM images for (a) $C_{16}SS\text{-}ZrO_2$ (b) $S\text{-}ZrO_2$ (c) $C_8S\text{-}ZrO_2$ (EtOH) (d) $C_8S\text{-}ZrO_2$ (IEE).

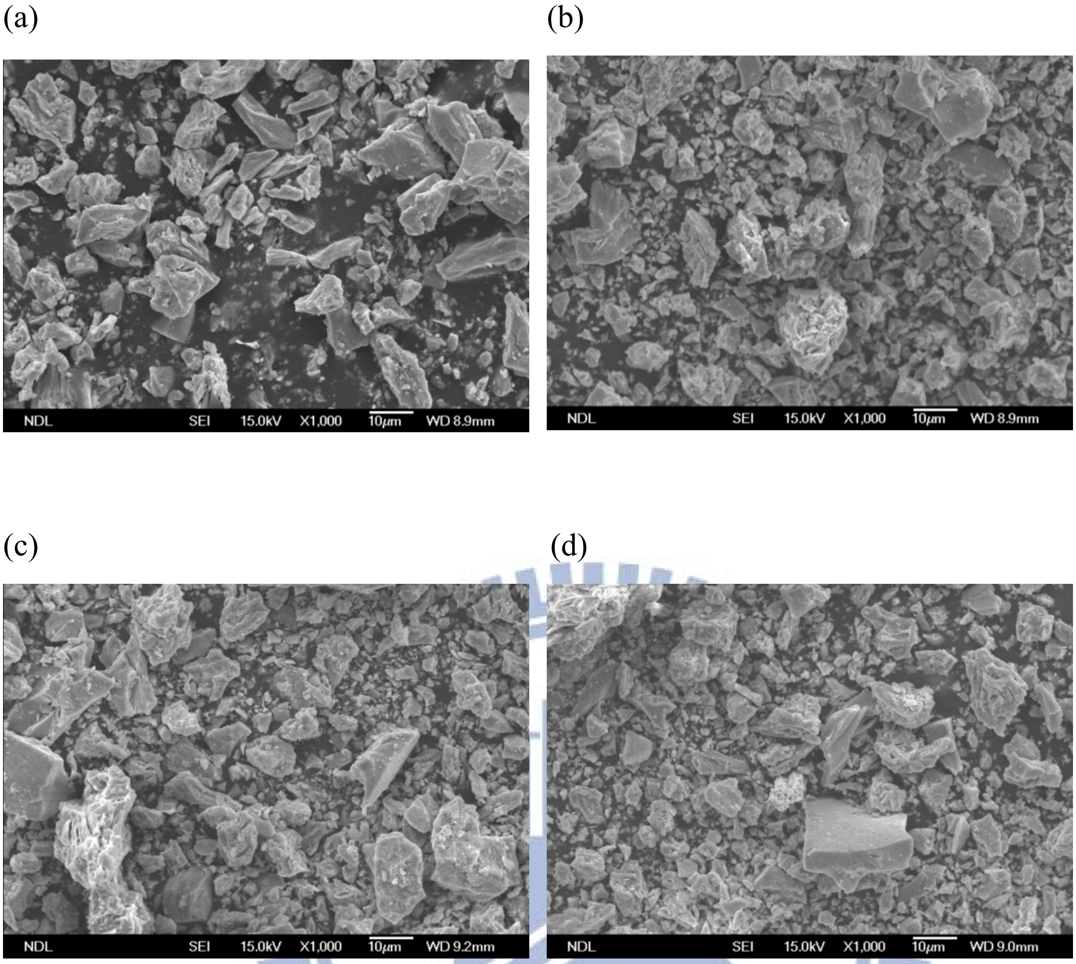

Appendix C-3 SEM images for the $C_{16}S$-ZrO_2 impregnated with sulfuric acid at different concentrations. (a) $C_{16}S$-ZrO_2 - 0.3M (b) $C_{16}S$-ZrO_2 - 0.6M (c) $C_{16}S$-ZrO_2 - 0.9M (d) $C_{16}S$-ZrO_2 - 1.2M.

Appendix D. Water content of $C_{16}S\text{-}ZrO_2$ series samples

Appendix D-1. The water content, proton conductivity and pore size of the $C_{16}S\text{-}ZrO_2$ series samples

CTAB/Zr molar ratio	**WC_{total} (RT-400°C)**	**$WC_{100\text{-}400}$ (100-400°C)**	**$WC_{100\text{-}400}/WC_{total}$ ($\times 10^{-2}$)**	**Proton Conductivity (mS/cm)**	**Pore diameter (nm)**
0.25	21.5% [a]	3.3%	15.3	12	8.2
0.38	23.8%	4.2%	17.6	16	2.4
0.50	27.4%	5.1%	18.6	20	2.8
0.63	18.9%	3.2%	16.9	17	3.0

a- weight loss%

Appendix E. NH_3 TPD samples weight and patterns

Appendix E-1. The weight of the sulfated ZrO_2 sample

Sample	Weight (g)
S-ZrO_2	0.1260
C_{16}S-ZrO_2	0.1235
C_{16}SS-ZrO_2	0.1224
C_{16}S-ZrO_2-0.3M	0.1256
C_{16}S-ZrO_2-0.6M	0.1256
C_{16}S-ZrO_2-0.9M	0.1263
C_{16}S-ZrO_2-1.2M	0.1248
C_8S-ZrO_2(IEE)	0.1230
C_8S-ZrO_2(EtOH)	0.1225

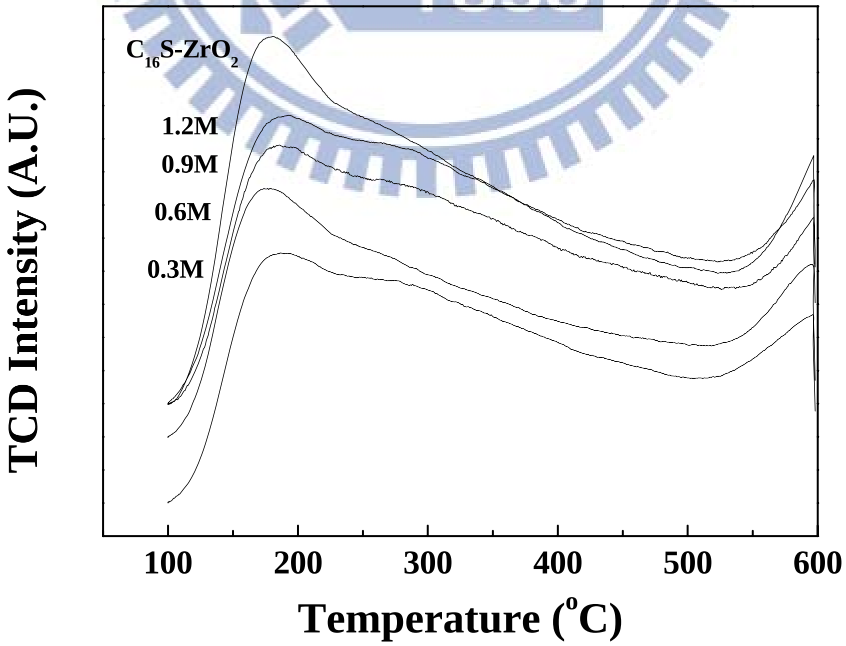

Appendix E-2. The NH_3 TPD patterns for the C_{16}S-ZrO_2 series samples

Appendix F. TEM images of sulfated ZrO_2

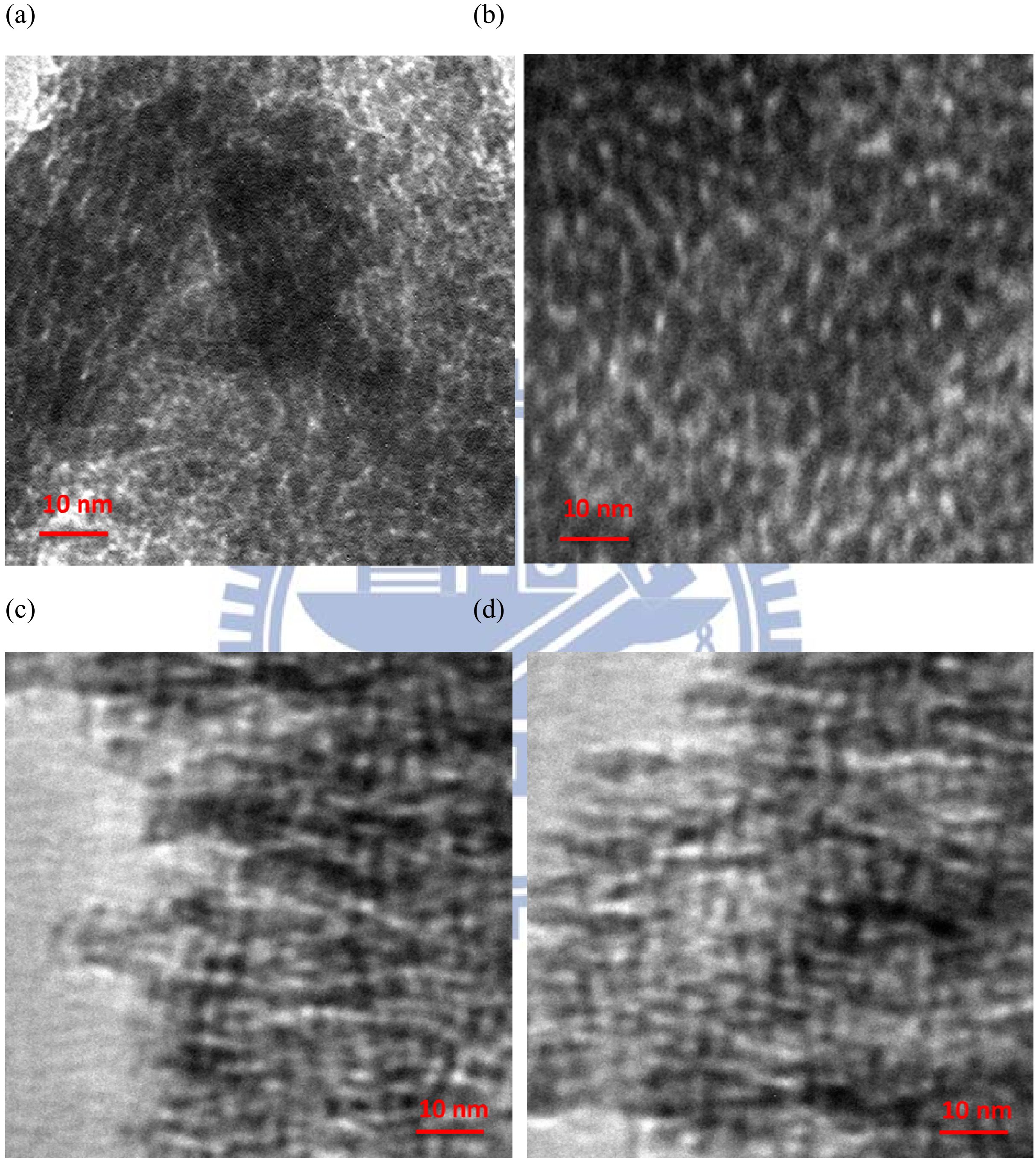

Appendix F-1 TEM images for (a) $C_{16}S\text{-}ZrO_2$ (b) $C_{16}SS\text{-}ZrO_2$ (c) $C_8S\text{-}ZrO_2$ (EtOH) (d) $C_8S\text{-}ZrO_2$ (IEE).

(a) (b)

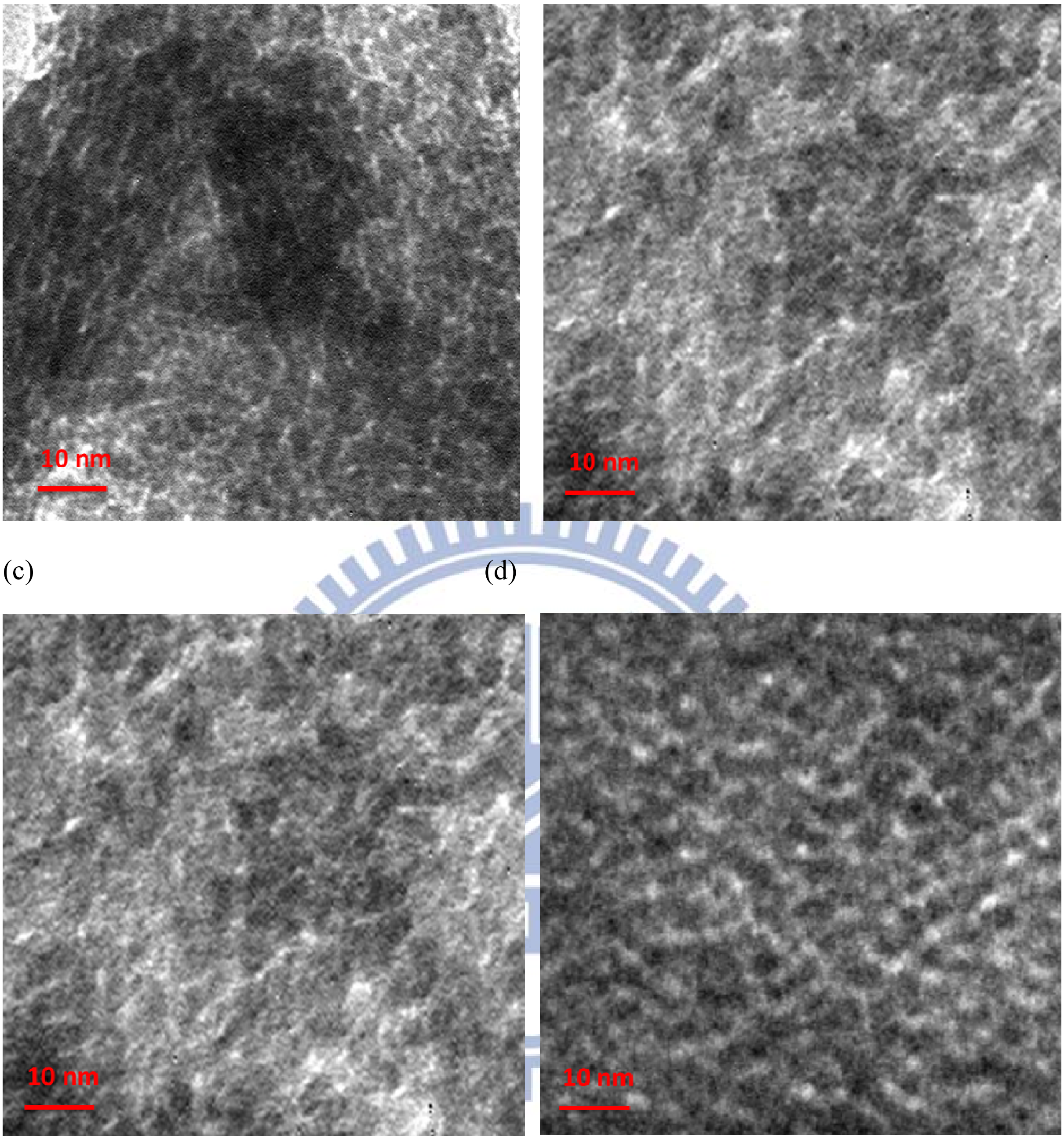

Appendix F-2 TEM images for the $C_{16}S\text{-}ZrO_2$ impregnated with sulfuric acid at different concentrations. (a) $C_{16}S\text{-}ZrO_2$ - 0.3M (b) $C_{16}S\text{-}ZrO_2$ - 0.6M (c) $C_{16}S\text{-}ZrO_2$ - 0.9M (d) $C_{16}S\text{-}ZrO_2$ - 1.2M.